ALGORITHM THEORETICAL BASIS DOCUMENT FOR MSG SEVIRI FIRE RADIATIVE POWER (FRP) CHARACTERISATION

FRP: LSA-502 (FRP-PIXEL), LSA-503 (FRP-GRID), LSA-550(FRP-PIXEL-R), LSA-551 (FRP-GRID-R).

The EUMETSAT Network of Satellite Application Facilities

LSA SAF
Land Surface Analysis

Prepared by

Y. GOVAERTS[1], M. WOOSTER[2], G. ROBERTS[2], P. FREEBORN[2], W. XU[2], J. He[2] and A. LATTANZIO[3]

(1) EUMETSAT; (2) King's College London; (3) Makalumedia

Document issue	**:**	FRP VERSION 2.8
Doc No	**:**	**EUM/MET/SPE/06/0398**
FRPPixel (LSA-31)algorithm version	**:**	**2.0**
FRPPixel (LSA-32)algorithm version	**:**	**2.0**
Date	**:**	**October 2015**

Document Change Record

Doc. Issue	Algo. Pxl	Algo. Grd	Date	Remarks
1.0			June 2006	Original King's College London version
1.1			October 2006	Version prototyped at EUMETSAT.
1.2	0.16		May 2007	First version delivered at IM. FRE estimation has been removed.
2.0	0.8	0.16	March 2008	Version prepared for the Operation Readiness Review. Include the gridded FRP product estimation that includes a correction for the undetected small fires.
2.1	0.9	0.16	June 2008	Include the reply to the comments raised for the ORR3.
2.2	1.1	0.16	June 2009	Include the modifications for the ORR3 close-out, *i.e.*, (1) improved definition of the atmospheric correction, (2) saturated radiances are assigned a default value, (3) improved estimation of FRP error estimation (Equation 50), (4) changes of the units.
2.3	1.2	0.16	July 2009	Changes following the ORR3 close-out meeting: (1) change the title page, (2) update the list of assumptions, (3) add new error fields in the product file.
2.4	1.3	0.3	September 2009	Changes for the preparation of the FRPGrid product ORR. A new method is used for the small fire correction. A method has been added for the FRPGrid error estimation..
2.5	1.3	0.4	October 2009	Modification of section 3.9.1 and adding of section 4.3.
2.6	1.3	0.4	January 2010	Modification of Sections 3.9 and 4.3 for the FRP GRIDDED closeout.
2.7	1.3	0.4	March 2014	Added short paragraph to introduction to state which products this ATBD is applicable to.
2.8	2.0	2.0	October 2015	Including the modifications for porting the FRP c code into Python: (1) clarify the description of SAF NWC cloud mask modification; (2) atmosphere correction coefficient from MODTRAN; (3) take off cloud edge test.

Table of Contents

List of Acronyms

ATBD	Algorithm Theoretical Basis Document
ATSR	Along Track Scanning Radiometer
BT	Brightness Temperature
CLM	CLoud Mask (MPEF product)
FIR	Finite Impulse Response
FRP	Fire Radiative Power
FRE	Fire Radiative Energy
HRV	High Resolution Visible
LSA	Land SAF
LUT	Look-Up Table
LWIR	Longwave InfraRed
MAD	Mean Absolute Deviation
MIR	Middle InfraRed
MODIS	Moderate-Resolution Imaging Spectroradiometer
MPEF	Meteorological Product Extraction Facility
ORR	Operation Readiness Review
PSF	Point Spread Function
ROI	Region of Interest
SAF	Satellite Application Facility
SEVIRI	Spinning Enhanced Visible and InfraRed Imager
SSP	Sub-Satellite Point
TIR	Thermal InfraRed
TOA	Top Of Atmosphere
TRMM	Tropical Rainfall Measuring Mission
VIRS	Visible and Infrared Spectrometer

List of Symbols

Generic notations		
$\breve{x}$		mean absolute deviation of x
$\overline{x}$		Mean value of x
$\widetilde{x}$		Spectrally integraed value of x
$\widehat{x}$		Temporally integrated value of x
$\mathbf{X}$		Matrix
I	$\mathrm{mWm^{-2}sr^{-1}(cm^{-1})^{-1}}$	Spectral radiance
$\widetilde{I}$	$\mathrm{mWm^{-2}sr^{-1}}$	Spectrally integrated radiance
L	$\mathrm{mWm^{-2}sr^{-1}}$	Radiance
F	$\mathrm{mWm^{-2}(cm^{-1})^{-1}}$	Spectral flux
$\widetilde{F}$	$\mathrm{mWm^{-2}}$	Flux within a spectral interval
T	K	Temperature
C		Constant value
Γ		Threshold value
Λ		Transmittance
ϵ		Emissivity
λ	μm	Wavelength
ν	$\mathrm{cm^{-1}}$	Wavenumber
τ		Optical thickness

Geometry		
θ_g	degree	Sunglint angle
θ_s	degree	Sun zenith angle
ϕ_s	degree	Sun azimuth angle
Ω_s	degree	Sun direction : (μ_s, ϕ_s)
θ_v	degree	Viewing zenith angle
ϕ_v	degree	Viewing azimuth angle
Ω_v	degree	Viewing direction : (μ_v, ϕ_v)
ϕ_r	degree	Relative azimuth angle : $\phi_v - \phi_s$
Ω	degree	Sun and viewing direction : $\mu_s, -\mu_v, \phi_r$
$\mu_{s,v}$		cosine of angle

FRP/GFRP Latin upper case		
A_0	m^2	Pixel area at the sub-satellite point
A_f	m^2	Fire area
A_s	m^2	Pixel area
B_t	K	Brightness temperature
C_s		Scaling constant
F_f	$mWm^{-2}sr^{-1}(cm^{-1})^{-1}$	Fire emitted spectral flux
I_f	$mWm^{-2}sr^{-1}(cm^{-1})^{-1}$	Fire emitted spectral radiance
I_b	$mWm^{-2}sr^{-1}(cm^{-1})^{-1}$	Background spectral radiance
$\mathbf{K}$		Matrix defining the high pass filter
N_b		Number of valid background pixels
N_c		Number of cloudy pixels in $\mathbf{W}_b$
N_k		Number of fire components
N_s		Total number of pixels in $\mathbf{W}_b$
N_t		Total number of valid values used for the GFRP estimation
N_w		Number of water pixels in $\mathbf{W}_b$
$\widetilde{R}_P$	W	Estimated fire Radiative Power
T_b	K	Background temperature
T_f	K	Fire temperature
U_{H_2O}	kg/m^2	Water vapour concentration
U_{O_3}	DU	Ozone concentration
U_{CO_2}	ppmv	Surface CO_2 concentration
$\mathbf{W}_b$		Background pixel matrix
$\mathcal{B}$		Ensemble of valid background pixels
$\mathcal{F}$		Theoretical magnitude-frequency ditribution of FRP values
$\mathcal{H}$		Actual magnitude-frequency ditribution of FRP values
$\mathcal{P}_f$		Ensemble of potential fire pixels

FRP/GFRP Latin lower case		
f_K		Size high pass filter matrix
f_s		Fraction of clear sky pixels in a regular grid box
h_K	K	Value of the high pass filter
i		Land surface clear-sky pixel column number
j		Land surface clear-sky pixel line number
i_b		Background pixel column number
j_b		Background pixel line number
i_f		Potential fire pixel column number
j_f		Potential fire pixel line number
i_G		Grid column number
j_G		Grid line number
k		Fire component
p_c		Coefficient to adjust the Γ_{VR} threshold value
s_b		Size of the background window $\mathbf{W}_b$
t	s	Time of acquisition
t_e	s	Time of the gridded FRP product generation
z_0		Bottom of the atmosphere
z_a		Top of the atmosphere

FRP/GFRP Greek		
α_c		Correction factor for undetected small fires
β_c		Power factor for undetected small fires
Δ_B	K	Brightness temperature difference
ϵ_f		Fire emissivity
σ_b		Atmospheric correction error resulting from atmospheric compositon uncertainty
$\sigma_{\mathrm{H_2O}}$		Atmospheric correction error resulting from H_2O concentration uncertainty
σ_h	K	Standard deviation of h_K
σ_{SB}	$\mathrm{mWm^{-2}K^{-4}}$	Stefan-Boltzmann constant
$\sigma_{\widetilde{I}_b}$	$\mathrm{mWm^{-2}sr^{-1}(cm^{-1})^{-1}}$	Standard deviation of $\widetilde{I}_b$
Γ_I	K	Estimated threshold value for fire identification
Γ_Δ	K	Estimated threshold value for fire identification
Γ_h	K	Estimated threshold value for fire identification
Λ'_a		Total atmospheric pseudo-transmittance
Λ_a		Total atmospheric transmittance
Λ_g		Total gaseous transmittance
τ_a		Total atmospheric optical thickness
τ_g		Total gaseous optical thickness

1 INTRODUCTION

1.1 Purpose

This document details the algorithm used for the retrieval of Fire Radiative Power (FRP) from the Spinning Enhanced Visible and Infrared Imager (SEVIRI) onboard Meteosat Second Generation (MSG) satellites. The sections below describe the theoretical basis for active fire detection and FRP estimation, together with the processing of the respective error budget. The methodology detailed here applies to near real time FRP products - FRP-PIXEL with product identifier LSA-502 and FRP-GRID with product identifier LSA-503 as well as to the re-processed FRP datasets (FRP-PIXEL-R) with product identifier LSA-550 and FRP-GRID-R with product identifier LSA-551. A peer reviewed paper (Wooster et al., 2015) describes the algorithm in full and should be referred to in publications that use the LSA SAF FRP products generated from SEVIRI data.

Biomass burning is a key component of Earth's biogeochemical cycle, and a major source of trace gas and aerosol emissions to the atmosphere (Andreae 1991). Burning is most widespread in tropical regions, including in Africa where Savannah fires are believed to account for almost one third of global burning emissions (Andreae 1991). These emissions include species that have the potential for radiative forcing of climate, including smoke aerosol, CO_2, and precursors to tropospheric ozone. In terms of CO_2, it has been estimated that the magnitude of global emissions may approach those due to fossil fuel burning, though much of this will be re-sequested by post-fire vegetation re-growth. Nevertheless, whilst fossil fuel CO_2 emissions are increasing steadily each year, atmospheric CO_2 increase is subject to large inter-annual variations and differences in the regional and global prevalence of fire is understood to be one factor accounting for this variation. Thus fire must be taken into account when attempting to understand current and future changes in the atmospheric CO_2 concentration, in addition to other climatologically important phenomena such as land-use and albedo change in the tropics (Govaerts et al. 2002) and radiative forcing by smoke aerosols and their interactions with clouds (Kirkevag et al. 1991). Due to the widespread nature of biomass burning, Earth Observation satellites data are seen as key to providing data on this phenomena for studies of climate perturbations and atmospheric chemistry (Schultz 2002), and operators of instruments such as ATSR, MODIS and TRMM-VIRS have already developed biomass burning products for use in such research (Justice et al. 2002,Giglio et al. 2003).

The key variable used to assess the effects of a biomass burning event, or series of events, is the amount of fuel burned (Scholes et al. 1996), generally derived using an equation of the form:

$$M = A_1 \; A_2 \; A_3 \tag{1}$$

where M is the amount of dry biomass combusted (kg), A_1 is the burnt area (m^2), A_2 is the biomass density (kg/m^2) and A_3 is the combustion factor (*i.e.*, the fraction of the available fuel actually consumed, unitless). Estimation of burned area has received much attention and useable satellite-derived products available at the continental scale are now becoming available. However, the related remote sensing estimates of biomass density and combustion efficiency are not foreseen in the near term, leading to large uncertainties in parameterisation of (1). Due to these limitations an alternative, independent approach to estimating M was considered by (Kaufman et al. 1996,Kaufman et al. 1998) for use with the MODIS Airborne Simulator, and later the MODIS spaceborne instrument, based on analysis of the fires whilst they are still actively burning. Essentially, it was hypothesised that the amount of radiant energy liberated per unit time during a burn (the so-called Fire Radiative Power) should relate to the rate at which the fuel is being consumed. Wooster (2002) and Wooster et al. (2003) developed the approach further, indicating that temporal integration of this Fire Radiative Power (FRP) measure over the lifetime of the burn provides a measure of the total Fire Radiative Energy (FRE), which should be proportional

to the fuel mass combusted. Observations from a geostationary platform would provide the temporally detailed record necessary to undertake this temporal integration, and the measurement of FRE represents an alternative, physically-based variable capable of being used to provide an independent estimate of parameter M in Equation (1), assuming that the amount of radiated energy released per kg of fuel mass burned (the so-called radiative heat yield of the fuel) is known.

1.2 Scope

This document describes the theoretical basis of the Fire Radiative Power characterisation algorithm used for the generation of the Fire Radiative Power (FRP-PIXEL) derived at the SEVIRI pixel resolution and Gridded Fire Radiative Power (FRP-GRID) derived on a hourly basis on a $5^\circ \times 5^\circ$ grid products from SEVIRI observations, full details can be found in Wooster et al., (2015) .

2 OVERVIEW

2.1 Objectives

The main objective of the FRP algorithm is the estimation of the FRP and FRP Gridded values from SEVIRI observations. Wein's displacement Law indicates that the peak of thermal emission from vegetation fires (which are generally dominated by burning at temperatures between 600 K and 1300 K) occurs in the Middle Infrared (MIR) (3 – 5 μm) spectral region. At the SEVIRI MIR channel central wavelength (3.9 μm), the thermal radiation emitted by such fires can be up to four orders of magnitude more intense than that from the ambient background. This intense thermal emission means that pixels containing actively burning fires can be discriminated via their significant increase in MIR pixel brightness temperature, even if the fire covers only 10^{-3} – 10^{-4} of the pixel planimetric area.

2.2 Retrieval strategy

As previously described, the Fire Radiative Power (FRP) measure quantifies the rate of release of radiant energy by a fire over all wavelengths. However, imaging sensors such as SEVIRI measure thermal radiation in only discrete wavebands. Two traditional approaches to address the estimation of FRP from such data are the Bi-spectral method coupled to the Stefan-Boltzmann Law (Dozier 1981), and an alternative approach used within the MODIS fire products (Justice et al. 2002). A third method for retrieving FRP, developed in part specifically for use with SEVIRI, is the MIR radiance method (Wooster et al. 2003). This approach approximates the Planck function relationship between the emitted spectral radiance and the emitter temperature by a simple power law. The method exploits the fact that for the temperature range of active fires and for wavebands in the MIR spectral region, an exponent in this approximation approaches that found in Stefan's Law, which itself relates total emitted radiance over all wavelengths (*i.e.*, the Fire Radiative Power) to emitter temperature.

The first stage in deriving FRP measures from SEVIRI radiance measures is detection of the active fire pixels, based mainly on their significant impact on the MIR spectral channel. The type of fire detection algorithm proposed for use with SEVIRI is based on the principles applied to generate active fire detections within the MODIS Fire Products (Giglio et al. 2003). The algorithm works on statistics derived primarily from the MIR and Thermal Infrared (TIR1) brightness temperature images, and their differences. On a first pass a series of absolute thresholds applied to these data are used to detect "potential" fire pixels, which are then further assessed as true or false fire detections based on a series of

further "contextual" tests whose thresholds are based on statistics derived from immediately neighbouring non-fire "background" pixels. Background pixel statistics are obtained from a window surrounding each potential fire pixel, commencing as a 5×5 matrix and being expanded until a given percentage of the window pixels are not themselves classed as potential fire pixels. Each potential fire pixel must pass all tests to be confirmed as a "true" fire pixel. Specular reflections from undetected cloud can present a similar signature to fires under certain daytime conditions (Giglio et al. 2003), so a cloud mask is used to remove cloud-contaminated pixels. The assumptions and limitations of the FRP algorithm are summarised in Section (4).

The FRP-GRID product is derived at regular interval, typically one hour, on a regular lat/lon grid. The spatial resolution of SEVIRI prevents the detection fire of limited intensity. Hence, a correction factor is applied on the FRP-GRID product to minimize this effect.

2.3 Delivered products

The FRP algorithm computes the FRP of each processed pixel for every available slots, the associated retrieval error and a quality indicator indicating the confidence in the retrieval. These values are also delivered on a $5^\circ \times 5^\circ$ degree resolution. This latter value is temporally averaged to provide the FRP at this spatial and temporal resolutions. The list of fields included in these two products are given in Annex (B).

3 ALGORITHM DESCRIPTION

3.1 Physics of the problem

The temperature of an active fire typically varies from around 675K for smoldering wood up to perhaps 1600K in the flaming zone. The emitted spectral radiance I_f (mWm^{-2}sr^{-1}(cm^{-1})$^{-1}$) at wavenumber ν in the viewing direction Ω_v from a fire at temperature T_f is given by

$$I_f(\Omega_v, \nu, z_0; T_f) = \epsilon_f(\Omega_v, \nu)\, B(\nu, T_f) \tag{2}$$

where $\epsilon_f(\Omega_v, \nu)$ is the fire emissivity at wavenumber ν in the direction Ω_v, $B(\nu, T_f)$ is the Planck function (mWm^{-2}sr^{-1}(cm^{-1})$^{-1}$) and z_0 denotes the bottom of the atmosphere. In this Equation and all the subsequent ones, the variables appearing at the left side of the semicolon symbol denote those variables which are independent from the observed medium whereas those appearing at right side of this symbol determine the radiative properties of this medium. The total spectral fire radiative power F_f (mWm^{-2}(cm^{-1})$^{-1}$) is thus

$$F_f(\nu, z_0; T_f) = \int_{2\pi} I_f(\Omega_v, \nu, z_0; T_f)\, \cos\theta_v d\Omega_v. \tag{3}$$

with $d\Omega_v = \sin\theta d\theta d\phi$. The fire radiative power at temperature T_f emitted over the entire spectrum $\widetilde{F}_f(z_0; T_f)$ (mWm^{-2}) writes thus

$$\widetilde{F}_f(z_0; T_f) = \int_0^\infty F_f(\nu, z_0; T_f)\, d\nu. \tag{4}$$

When the emissivity is equal to 1, *i.e.*, blackbody, this equation becomes

$$\widetilde{F}_f(z_0; T_f) = \sigma_{SB} T_f^4 \tag{5}$$

where σ_{SB} is the Stefan-Boltzmann constant (Js^{-1}m^{-2}K^{-4}). When the fire emissivity is smaller than one, this equation becomes

$$\widetilde{F}_f(z_0;T_f) = \epsilon_f \, \sigma_{SB} T_f^4 \tag{6}$$

assuming that the emissivity ϵ_f takes a constant value over the spectral domain of integration. When ϵ_f exhibits some spectral variations, Equation (6) does not hold anymore and Equation (4) should be used instead. However, to ease the computation, Equation (4) can be approximated by

$$\widetilde{F}_f(z_0;T_f) \approx \widetilde{\epsilon}_f \sigma_{SB} T_f^4 \tag{7}$$

with

$$\widetilde{\epsilon}_f = \frac{1}{\widetilde{B}(T_f)} \int_0^\infty \epsilon_f(\nu) \; B(\nu, T_f) \; d\nu. \tag{8}$$

A single wildfire is likely to consist of multiple flaming and smoldering zones with a range of temperatures fluctuating at small spatial scales. The fire radiative power $\widetilde{F}_f(z_0;T_f)$ (Wm^{-2}) of such a fire can be expressed by

$$\widetilde{F}_f(z_0;T_f) \approx \widetilde{\epsilon}_f \, \sigma_{SB} \sum_{k=1}^{N_f} A_f(k) \, T_k^4 \tag{9}$$

where $A_f(k)$ is the fire area of the k surface thermal component within the field-of-view, N_f is the number of temperature components in the fire and T_k is the kinetic temperature (K) of the thermal component k.

Deriving $\widetilde{F}_f(z_0;T_f)$ from space observations raises several issues. Equation (9) describes the total fire radiative power in all directions over an extended spectral range whereas space-borne radiometers typically measure radiance in a given direction and in a discrete spectral interval. Additionally, the field-of-view of radiometers like SEVIRI are much larger than the fire size so that the observed pixel brightness temperature is significant lower than the actual fire brightness temperature. It is also assumed that the released thermal radiation is uniformly emitted in all viewing directions so that Equation (3) can be easily solved.

U_{H_2O} kg/m^2	U_{O_3} DU	U_{CO_2} ppmv	Λ_{H_2O}	Λ_{O_3}	Λ_{CO_2}	Λ_g
20	354	330	0.944	1.000	0.802	0.748
20	354	360	0.944	1.000	0.801	0.747
20	354	390	0.944	1.000	0.800	0.746
10	354	360	0.969	1.000	0.800	0.771
30	354	360	0.922	1.000	0.801	0.727
60	354	360	0.861	1.000	0.801	0.675

Table 1: Typical gaseous transmittances along the vertical in the λ_{MIR} spectral band for different concentrations. Λ_g is the total gaseous transmittance.

The issue concerning the spectral range is addressed following the single waveband approach proposed by Wooster et al. (2003). This approach is based on a simple approximation of Equation (7) and relies on quantification of the fire pixel and ambient background pixel signal in only one spectral channel, namely the MIR band. It is assumed that the Planck's radiation law is well approximated by a fourth order power law for wavelengths in the 3.4 – 4.2 μm atmospheric window and the temperatures predominating in

active fires. This assumption introduces a $\pm 12\%$ relative error in the FRP estimation for fires lying within temperature range 665 – 1365 k (Wooster et al. 2005, Fig. 2). Accordingly, the emitted spectral flux of a fire can be approximated by

$$\widetilde{F}_f(z_0, \nu_{MIR}; T_f) \approx pi\, \widetilde{\epsilon}_f(\nu_{MIR})\, \widetilde{B}(\nu_{MIR}, T_f) \approx \widetilde{\epsilon}_f(\nu_{MIR})\, C_a(\nu_{MIR})\, T_f^4 \tag{10}$$

where $C_a(\nu_{MIR})$ is a constant ($\mathrm{mWm^{-2}K^{-4}}$) which depends upon the actual range of the MIR spectral interval. This power law relation is identical in form to the Stefan-Boltzmann law (Equation 7) and equating these two relations allows the dependance upon emitter temperature to be removed and the true fire thermal emission over the entire spectrum to be estimated directly from the fire-emitted MIR spectral radiance, without knowledge of the fire temperature or temperature distribution. Under these conditions, Equation (9) becomes

$$\widetilde{R}_P = \frac{\pi\, A_f\, \sigma_{SB}\, \widetilde{\epsilon}_f}{C_a(\nu_{MIR})\, \widetilde{\epsilon}_f(\nu_{MIR})}\, \widetilde{F}_f(z_0, \nu_{MIR}; T_f) \tag{11}$$

Assuming that $\widetilde{\epsilon}_f = \widetilde{\epsilon}_f(\nu_{MIR})$, the FRP can be expressed by

$$\widetilde{R}_P = \frac{\pi\, A_f\, \sigma_{SB}}{C_a(\nu_{MIR})}\, \widetilde{F}_f(z_0, \nu_{MIR}; T_f). \tag{12}$$

An instrument like SEVIRI does not observe fires that encompass the entire field-of-view, but only a very limited fraction of it. The radiance actually observed at the satellite level z_a in the λ_{MIR} spectral band over a pixel affected by a fire can be expressed as the contribution of the emitted/reflected radiance over the fire and non-fire (background) area

$$\begin{aligned}
\widetilde{I}(\Omega_s, \Omega_v, \nu_{MIR}, t, z_a; T_b, T_f, \epsilon_f, p_f, \tau_a) \;=\; & p_f\, \Lambda_a^{\uparrow}(\Omega_v, \nu_{MIR}) \Big[\widetilde{\epsilon}_f(\nu_{MIR})\, \widetilde{B}(\nu_{MIR}, T_f) + \\
& \Big(1 - \widetilde{\epsilon}_f(\nu_{MIR})\Big) \Big(\widetilde{I}_0^{\downarrow}(\mu_s, \nu_{MIR}, z_0, t) \Lambda_a^{\downarrow}(\mu_s, \nu_{MIR}) + \widetilde{I}_a^{\downarrow}(\mu_s, \nu_{MIR}, z_0, t)) \Big) \Big] + \\
& (1 - p_f)\, \Lambda_a^{\uparrow}(\nu_{MIR}) \Big[\widetilde{\epsilon}_b(\nu_{MIR})\, \widetilde{B}(\nu_{MIR}, T_b) + \\
& \Big(1 - \widetilde{\epsilon}_b(\nu_{MIR})\Big) \Big(\widetilde{I}_0^{\downarrow}(\mu_s, \nu_{MIR}, z_0, t) \Lambda_a^{\downarrow}(\nu_{MIR}) + \widetilde{I}_a^{\downarrow}(\mu_s, \nu_{MIR}, z_0, t)) \Big) \Big] + \\
& \widetilde{I}_a^{\uparrow}(\Omega_v, \nu_{MIR}, z_a, t)
\end{aligned} \tag{13}$$

where

p_f	pixel fraction affected by fire
T_f	fire temperature
T_b	background surface temperature
$\widetilde{I}_0^{\downarrow}$	solar direct downwelling radiance
$\Lambda_a^{\uparrow}$	upwelling atmospheric transmission
$\Lambda_a^{\downarrow}$	direct downwelling transmittance
$\widetilde{I}_a^{\downarrow}$	diffuse downwelling atmospheric radiance
$\widetilde{\epsilon}_b$	background surface emissivity
$\widetilde{I}_a^{\uparrow}$	atmospheric total upward radiance

According to Wooster et al. (2005) $\epsilon_f = 1$ so that there is no reflected contribution above the fires, equation (13) writes

$$\widetilde{I}(\Omega_s, \Omega_v, \nu_{MIR}, t, z_a; T_b, T_f, \epsilon_f, p_f, \tau_g) \;=\; p_f\, \Lambda_a^{\uparrow}(\Omega_v, \nu_{MIR})\, \widetilde{\epsilon}_f(\nu_{MIR})\, \widetilde{B}(\nu_{MIR}, T_f) +$$

$$(1-p_f)\,\Lambda_a^{\uparrow}(\nu_{MIR})\Big[\widetilde{\epsilon}_b(\nu_{MIR})\,\widetilde{B}(\nu_{MIR},T_b)+ \Big(1-\widetilde{\epsilon}_b(\nu_{MIR})\Big)\Big(\widetilde{I}_0^{\downarrow}(\mu_s,\nu_{MIR},z_0,t)\Lambda_a^{\downarrow}(\nu_{MIR})+\widetilde{I}_a^{\downarrow}(\mu_s,\nu_{MIR},z_0,t)\Big)\Big]+ \widetilde{I}_a^{\uparrow}(\Omega_v,\nu_{MIR},z_a,t) \quad (14)$$

From Equations (3) and (14), and assuming that the atmospheric contribution $\widetilde{I}_a^{\uparrow}$ coming from the fire area can be neglected, the radiance emitted by the fire in the spectral interval λ_{MIR} in the direction Ω_v is expressed by

$$\begin{aligned}\widetilde{I}_f(\Omega_s,\Omega_v,\nu_{MIR},z_0,t) &= p_f\widetilde{\epsilon}_f(\nu_{MIR})\,\widetilde{B}(\nu_{MIR},T_f)\\ &= \frac{1}{\Lambda_a}\Big\{\widetilde{I}(\Omega_s,\Omega_v,\nu_{MIR},t,z_a;T_b,T_f,\epsilon_f,p_f,\tau_g)-\\ &\quad (1-p_f)\,\Lambda_a^{\uparrow}(\nu_{MIR})\Big[\widetilde{\epsilon}_b(\nu_{MIR})\,\widetilde{B}(\nu_{MIR},T_b)+\\ &\quad \Big(1-\widetilde{\epsilon}_b(\nu_{MIR})\Big)\Big(\widetilde{I}_0^{\downarrow}(\mu_s,\nu_{MIR},z_0,t)\Lambda_a^{\downarrow}(\nu_{MIR})+\widetilde{I}_a^{\downarrow}(\mu_s,\nu_{MIR},z_0,t)\Big)\Big]-\\ &\quad \widetilde{I}_a^{\uparrow}(\Omega_v,\nu_{MIR},z_0,t)\Big\} \quad (15)\end{aligned}$$

Equation (15) can be further simplified assuming that the term $p_f \ll 1$ so that $(1-p_f)\approx 1$ and writes now

$$\widetilde{I}_f(\Omega_s,\Omega_v,\nu_{MIR},z_0,t,\tau_g)=\frac{1}{\Lambda_a^{\uparrow}(\nu_{MIR})}(\widetilde{I}(\Omega_s,\Omega_v,\nu_{MIR},t,z_a)-\widetilde{I}_b(\Omega_s,\Omega_v,\nu_{MIR},t,z_a)) \quad (16)$$

where

$$\begin{aligned}\widetilde{I}_b(\Omega_s,\Omega_v,\nu_{MIR},t,z_a) &= \Lambda_a^{\uparrow}(\nu_{MIR})\\ &\quad \Big[\widetilde{\epsilon}_b(\nu_{MIR})\,\widetilde{B}(\nu_{MIR},T_b)+\Big(1-\widetilde{\epsilon}_b(\nu_{MIR})\Big)\\ &\quad \Big(\widetilde{I}_0^{\downarrow}(\mu_s,\nu_{MIR},z_0,t)\Lambda_a^{\downarrow}(\nu_{MIR})+\widetilde{I}_a^{\downarrow}(\mu_s,\nu_{MIR},z_0,t)\Big)\Big]+\\ &\quad \widetilde{I}_a^{\uparrow}(\Omega_v,\nu_{MIR},z_0,t) \quad (17)\end{aligned}$$

is the background radiance field that would have been observed in the absence of fire. It is assumed that this value is determined from the clear sky surrounding pixels not affected by fires. Typical values of gaseous transmittances are given in Table (1). Combining Equations (12) and (16), the FRP is estimated with

$$\widetilde{R}_P(t)=\frac{A_s\,\sigma_{SB}}{C_a(\nu_{MIR})}\int_{2\pi}\widetilde{I}_f(\Omega_s,\Omega_v,\nu_{MIR},z_0,t;T_f)\,cos\theta_v\,d\Omega_v. \quad (18)$$

The estimation of $\widetilde{R}_P(t)$ requires the computation of Equations (16) and (18) for every processed pixels.

3.2 Algorithm overview

The main objective of the FRP algorithm is to deliver the $\widetilde{R}_P$ and the main values used to determined it. Equation (18) is solved for each pixel believed to be affected by fire. The following processing takes place for each SEVIRI pixel located within a Region Of Interest (ROI)

1. Clear sky pixel identification;
2. Potential fire identification;

3. Background pixel identification;
4. FRP assessment (including atmospheric correction);
5. FRP uncertainty estimation;
6. Quality flag estimation.

Processing steps three and beyond take place only for pixels that have been identified as potential fire pixels in step 2.

3.3 Clear sky pixel identification

The cloud mask is used to remove cloud-contaminated pixels. Currently, this cloud mask is derived from the method proposed by Derrien and Le Gleau (2005) (Section A.1.2). This cloud mask is however optimized to minimize the possibility to identify fire smoke as cloud. Specifically, the cloud pixels are re-classed as non-cloudy if their classification as cloud is based on either of the following three tests fully detailed in (MeteoFrance 2007): (i) the `LocalSpatialTexture` bit is set to 1 or (ii) the `T3.9-T10.8` bit is set to 1 or (iii) the `SpatialSmoothing` test bit, which fills in cloud detection 'gaps' in areas of semi-transparent cloud. If at least three pixels immediately surrounding a cloudy pixel were classed as cloudy based on this test, the pixel is reclassified as non-cloudy.

In order to further increase the reliability of this cloud mask, pixels fulfilling the following conditions are also flagged as cloudy:

$$B_t(\Omega_s, \Omega_v, \nu_{TIR1}, t, z_a, i, j) - B_t(\Omega_s, \Omega_v, \nu_{TIR2}, t, z_a, i, j) \;>\; \Gamma_{01} \tag{19}$$

$$I(\Omega_s, \Omega_v, \nu_{MIR}, t, z_a, i, j) \;/\; I(\Omega_s, \Omega_v, \nu_{VIS}, t, z_a, i, j) \;<\; \Gamma_{02} \tag{20}$$

$$B_t(\Omega_s, \Omega_v, \nu_{MIR}, t, z_a, i, j) - B_t(\Omega_s, \Omega_v, \nu_{TIR1}, t, z_a, i, j) \;>\; \Gamma_{03} \tag{21}$$

Pixels discounted by this series of cloud tests receive the `CLOUD` status flag value (see Annex B).

Finally, pixels located next to a "water" pixel are also disregarded from further processing. A water pixel is identified from the land/sea mask (see Annex A.2) and the test applies only to pixels which satisfy

$$B_t(\Omega_s, \Omega_v, \nu_{MIR}, t, z_a, i, j) \;<\; \Gamma_{04}. \tag{22}$$

Pixels discounted by the water edge test are flagged as `WATEREDGE` (see Annex B). This test is to limit the number of false detections which may result from water bodies. It also means that "true" fires will also go undetected next to water bodies, where the condition related to Equation (22) is satisfied. Previously pixels immediately next to clouds (i.e. cloud edge) pixels were also masked, but this has now been found to be unnecessary and is not longer conducted.

3.4 Potential fire detection

To speed-up the computation of Equations (16) and (18), pixels that are potentially affected by fires are first identified within the processed area. This first component is a trade off between computation speed/overhead and increased false detections on one hand and underestimation of fire activity and biomass burning on the other. If the conditions for selecting potential fire pixels are conservative fewer pixels will be returned which will reduce the prevalence of false detections whilst benefiting from reduced processing time. On the other hand, if the conditions are quite liberal a greater number of pixels

will be returned which has the inverse effect by increasing computational overhead and the likelihood of false detections.

The approach adopted in the FRP algorithm is to identify "potential" fire pixels using a liberal approach since an earlier comparison between SEVIRI and MODIS suggests SEVIRI misses a significant number of fires that MODIS detects. Whilst this is to be expected to some degree given the significantly lower spatial resolution of SEVIRI when compared to MODIS, it was deemed more important to increase the sensitivity of the SEVIRI FRP algorithm so that smaller fires could be detected whilst still attempting to minimize false detections. The determination of the ensemble of potential fire pixels relies on two series of tests applied only at clear sky pixels (i, j) over land surfaces:

1. This identification relies on a series of simple tests based on threshold values. These tests change according to daylight or nighttime conditions. Radiances in SEVIRI 3.9μm (referred to as MIR band) and 10.8μm (referred to as the TIR1 band) bands are first converted into brightness temperatures B_t and the difference $\Delta_B(t,i,j) = B_t(\Omega_s, \Omega_v, \nu_{MIR}, t, z_a, i, j) - B_t(\Omega_v, \nu_{TIR1}, t, z_a, i, j)$ between these two channels estimated. The following threshold values are estimated

$$\Gamma_I(\nu_{MIR}, t, i, j) = C_{11}\ \theta_s(t,i,j) + C_{12} \quad (23)$$

$$\Gamma_\Delta(t,i,j) = C_{21}\ \theta_s(t,i,j) + C_{22} \quad (24)$$

   The constant C_{12} and C_{22} take different values during daytime, *i.e.*, when $\theta_s < 90^\circ$ and night time. C_{12} and C_{22} are null when $\theta_s(t,i,j) \geq 90^\circ$. A pixel will be kept for further analysis if all the following conditions are true

$$\begin{aligned} \mathcal{P}_1(t,i,j) \in \{(B_t(\Omega_s, \Omega_v, \nu_{MIR}, t, z_a, i, j) &\geq \Gamma_I(\nu_{MIR}, t, i, j)) \cap \\ (\Delta_B(t,i,j) &\geq \Gamma_\Delta(t,i,j)) \cap \\ (\theta_g(t,i,j) &< \Gamma_{g1} \cup \Gamma_{g2} > \theta_g(t,i,j))\} \end{aligned} \quad (25)$$

   where $\theta_g(t,i,j)$ is the sunglint angle with

$$\theta_g = \cos^{-1}\Big((\cos(\theta_v)\sin(\theta_s)) - (\sin(\theta_v)\sin(\theta_s)\cos(\phi_r))\Big). \quad (26)$$

   Pixels fulfilling the condition $\theta_g(t,i,j) \in]\Gamma_{g1}, \Gamma_{g2}[$ are assigned the `SUNG` status flag.

2. Within each ROI, a spatial analysis is next performed on $\Delta_B(t,i,j)$ for all cloud free pixels over land surfaces. The overall aim of applying a high pass spatial filter is to exploit the high frequency spatial signature of active fires when imaged at the SEVIRI spatial resolution, in order to detect as many potential fire pixels as possible whilst trying to keep computational overhead to a minimum. Whilst it is believed important to attempt to detect low intensity fires, even at the expense of increasing computational overhead, if the spectral thresholds represented by the series of tests in Step 1. were applied alone (and the thresholds were set very low to detect low intensity fire pixels) then in some slots most of the cloud free land surface would be returned as potential fires. Hence, the high pass spatial filter is used to narrow down the set of potential fire pixels below that returned by the spectral threshold tests alone.

   A series of high pass filters $\mathbf{K}$ of respective size $f_K \times f_K$ are sequentially applied on $\Delta_B(t,i,j)$

$$h_K(t,i,j) = \sum_{k=1}^{F_h}\sum_{l=1}^{F_h} \Delta_B(t, i-k+1, j-l+1)\,\mathbf{K}(k,l) \quad (27)$$

   where f_K is the filter size (3, 5 and 7), $\mathbf{K}$ is the f_K by f_K kernel matrix.

A threshold

$$\Gamma_h(t,i,j) = C_{41}\,\theta_s(t,i,j) + C_{42} \tag{28}$$

is defined to attempt to reduce the number of lower frequency values which is based upon the solar zenith angle. The threshold $\Gamma_h(t,i,j)$ takes smaller value with increasing solar zenith angle so that at times of lower contrast (sunrise/sunset) the threshold is less conservative. Using the SZA as a means to vary the thresholds also attempts to reduce "steps" in the fire detection success which occur when the magnitude of a threshold are changed in one slot. Pixels which are greater than

$$\mathcal{P}_2(t,i,j) \in \{h_K(t,i,j) \geq \Gamma_h(t,i,j)\,\sigma_h(t)\} \tag{29}$$

are identified as potential fire pixels. $\sigma_h(t)$ is the standard deviation of h_K. A pixel of $\Delta_B(t,i,j)$ belongs to $\mathcal{P}_2$ if the condition $h_K(t,i,j) \geq \Gamma_h(i,j)\,\sigma_h(t)$ is valid for at least one of the three kernel size f_K.

Pixels belonging to $\{\mathcal{P}_1(t,i,j) \cap \mathcal{P}_2(t,i,j)\}$ but which are affected by sunglint are not considered for further processing. The sunglint test is carried out using two band ratios 3.9μm /0.6μm (radiances) and 3.9μm /10.8μm (radiances). The 3.9μm /0.6μm ratio test is used to indicate if a pixel elevated MIR radiance is due to solar reflected radiation (which will also affect the 0.6μm channel)" whilst the 3.9μm /10.8μm ratio is used to indicate whether a pixels elevated MIR radiance is due to a homogeneous warm surface (which will also affect the TIR1 signal).

Sunglint contaminated pixels and homogeneously warm (non-fire) surfaces will have low values of these ratios. Pixels fulfilling the following two conditions

$$\begin{aligned} \mathcal{P}_3(t,i,j) \in \{\widetilde{I}(\Omega_s,\Omega_v,\nu_{MIR},t,z_a,i_f,j_f) \,/\, \widetilde{I}(\Omega_s,\Omega_v,\nu_{VIS},t,z_a,i_f,j_f) &< \Gamma_{VR}/p_c \cap \\ (2-p_c)\,\widetilde{I}(\Omega_s,\Omega_v,\nu_{MIR},t,z_a,i_f,j_f) \,/\, \widetilde{I}(\Omega_v,\nu_{TIR1},t,z_a,i_f,j_f) &< \Gamma_{TRR}\} \end{aligned} \tag{30}$$

are considered as affected by sunglint. Pixels belonging to $\mathcal{P}_3(t,i,j)$ are flagged as `SUNGRATIO`. If there are no cloudy pixels in the region of the "potential" fire pixel the threshold value Γ_{VR} in the first test of Equation (30) is reduced and second test always true. These conditions are controlled by p_c which is set to 1 when the 15×15 pixel surrounding area contains cloudy pixels, and is set to 2 otherwise.

Thus, potential fire pixels are defined by the condition

$$\mathcal{P}_f(t,i_f,j_f) \in \{\{\mathcal{P}_1(t,i,j) \cap \mathcal{P}_2(t,i,j)\} - \mathcal{P}_3(t,i,j)\}. \tag{31}$$

All processed pixels that do not belong to $\mathcal{P}_f(t,i_f,j_f)$ and have not yet be assigned a flag status are flagged as `NOTPOT`.

3.5 Background pixel identification

Pixels surrounding a potential fire pixel belonging to $\mathcal{P}_f$ are used for the estimation of the background radiance $\widetilde{I}_b(\Omega_s,\Omega_v,\nu_{MIR},t,z_a,i_f,j_f)$. This approach assumes the closest pixels are the most similar to the "potential" fire in the absence of fire. Before the fire pixel is analysed an assessment of the number "valid" background pixels is carried out. A minimum number of background pixels are required in order to estimate the BT of the "fire" pixel in the absence of fire. If there are too few samples for reliable background characterisation the window is expanded. The background area initially starts as a 5×5 pixel window which is expanded up to a maximum of 15×15. If there are still insufficient samples to estimate the background characteristics the pixel is flagged as a no "background" potential fire. Due to

the effects of the point spread function (PSF) and digital filtering, the pixels immediately surrounding the fire pixel are not used to characterise the background since these could be "contaminated" by the fire pixel radiance.

The size of the background window $\mathbf{W}_b$ surrounding the potential fire pixel in $\mathcal{P}_f(i_f, j_f)$ is chosen to contain enough clear sky pixels. A cloud-free land pixel (i_b, j_b) is valid for the estimation of the background radiance if the following conditions are met (omitting the angular notation)

$$\begin{aligned}
\mathcal{B}(t, i_b, j_b) = & \\
\{B_t(\nu_{MIR}, t, z_a, i_b, j_b) &< \Gamma_F \cap \\
B_t(\nu_{MIR}, t, z_a, i_b, j_b) &< B_t(\nu_{MIR}, t, z_a, i_f, j_f) \cap \\
B_t(\nu_{MIR}, t, z_a, i_b, j_b) &> \Gamma_{PSF} \cap \\
\Delta_B(t, i_b, j_b) &< \Gamma_D \cap \\
\Delta_B(t, i_b, j_b) &< \breve{\Delta}_B(i_f, j_f) \cap \\
(\theta_g(t, i, j) &< \Gamma_{g1} \cup \Gamma_{g3} > \theta_g(t, i, j)) \cap \\
\widetilde{I}(\nu_{MIR}, t, z_a, i_b, j_b)/\widetilde{I}(\Omega_v, \nu_{TIR1}, t, z_a, i_b, j_b) &< \Gamma_{TRR}\}
\end{aligned} \tag{32}$$

where

i_b, j_b	pixel $\in W_b$
Γ_F	potential fire threshold value
Γ_{PSF}	PSF threshold value
Γ_D	Δ_B threshold value
Γ_{TRR}	threshold value for the $I(\Omega_s, \Omega_v, \nu_{MIR}, t, z_a, i_b, j_b)/\widetilde{I}(\Omega_v, \nu_{TIR1}, t, z_a, i_b, j_b))$ ratio

A test on the PSF effects is needed to account for the PSF negative lobe effect so pixels which are below Γ_{PSF} are not taken into account. This is only applied above a certain SZA since it would eliminate many pixels at night or high solar zenith. For this reason it is based on the minimum SZA over a large array of pixels sufficient to account for even the largest window size. At twilight or night Γ_{PSF} is set to zero.

The size of the background window $\mathbf{W}_b$ used in Equation (32) is increased until the number of pixels $N_b \in \mathcal{B}$ used to define the background radiance satisfies the following condition

$$N_b \geq N_s \, \Gamma_c \tag{33}$$

where $N_s = s_b^2 - 9$ is the total number of pixels of the background window $\mathbf{W}_b$ and Γ_c is the minimum percentage of valid pixels in the background window. When condition (33) is not satisfied, the status flag is set to `NOBCK`.

3.6 FRP assessment

When Equation (33) is true, the "potential" fire pixel is assessed relative to the background statistics. When a suitable number of background pixels are detected the statistics of these pixels are derived for $\widetilde{I}$, Δ_B and B_t. These statistics are the mean values (omitting the angular notation)

$$\overline{B}_t(\nu_{MIR}, t, z_a, i_f, j_f) = \frac{\sum_{(i_b, j_b) \in \mathcal{B}} B_t(\nu_{MIR}, t, z_a, i_b, j_b)}{N_B} \tag{34}$$

$$\overline{B}_t(\nu_{TIR1}, t, z_a, i_f, j_f) = \frac{\sum_{(i_b,j_b)\in\mathcal{B}} B_t(\nu_{TIR1}, t, z_a, i_b, j_b)}{N_B} \quad (35)$$

$$\overline{\Delta}_{Bb}(t, i_f, j_f) = \frac{\sum_{(i_b,j_b)\in\mathcal{B}} \Delta_B(t, i_b, j_b)}{N_B} \quad (36)$$

$$\overline{\widetilde{I}}_b(\nu_{MIR}, t, z_a, i_f, j_f) = \frac{\sum_{(i_b,j_b)\in\mathcal{B}} \widetilde{I}(\nu_{MIR}, z_a, i_b, j_b)}{N_B} \quad (37)$$

where $\overline{B}_t(\nu_{MIR}, z_a, i_f, j_f)$ is the mean background brightness temperature in band λ_{MIR} corresponding to the potential fire pixel (i_f, j_f). The corresponding mean absolute deviations (MAD) are computed next

$$\breve{B}_t(\nu_{MIR}, t, z_a, i_f, j_f) = \frac{1}{N_B} \sum_{(i_b,j_b)\in\mathcal{B}} |B_t(\nu_{MIR}, t, z_a, i_b, j_b) - \overline{B}_t(\nu_{MIR}, t, z_a, i_f, j_f)| \quad (38)$$

$$\breve{B}_t(\nu_{TIR1}, z_a, i_f, j_f) = \frac{1}{N_B} \sum_{(i_b,j_b)\in\mathcal{B}} |B_t(\nu_{TIR1}, t, z_a, i_b, j_b) - \overline{B}_t(\nu_{TIR1}, t, z_a, i_f, j_f)| \quad (39)$$

$$\breve{\Delta}_{Bb}(t, i_f, j_f) = \frac{1}{N_B} \sum_{(i_b,j_b)\in\mathcal{B}} |\Delta_B(t, i_b, j_b) - \overline{\Delta}_{Bb}(t, i_f, j_f)| \quad (40)$$

$$\breve{\widetilde{I}}_b(\nu_{MIR}, t, z_a, i_f, j_f) = \frac{1}{N_B} \sum_{(i_b,j_b)\in\mathcal{B}} |\widetilde{I}(\nu_{MIR}, t, z_a, i_b, j_b) - \overline{\widetilde{I}}_b(\nu_{MIR}, t, z_a, i_f, j_f)| \quad (41)$$

The MAD is computed instead of the standard deviation as this is more resistant to outliers.

A contextual method similar to this employed in the MODIS algorithm (Giglio et al. 2003) is used to determine if a potential fire pixel should be confirmed as a true fire pixel. The mean and MAD of the background pixels for a given spectral channel/difference is used to assess if the potential fire pixel is sufficiently elevated above the background to be classed as a true fire. Three tests are applied to determine if a potential fire pixel is sufficiently above the background temperature. The tests on Δ_B are:

$$\Delta_B(t, i_f, j_f) \geq \overline{\Delta}_{Bb}(t, i_f, j_f) + C_{\Delta 1}\, \breve{\Delta}_{Bb}(t, i_f, j_f) \quad (42)$$

$$\Delta_B(t, i_f, j_f) \geq \overline{\Delta}_{Bb}(t, i_f, j_f) + C_{\Delta 2} \quad (43)$$

The test on $B_t(\lambda_{MIR})$ depends on the magnitude of $\breve{B}_t(\nu_{MIR}, t, z_a, i_f, j_f)$. When $\breve{B}_t(\nu_{MIR}, t, z_a, i_f, j_f) < 1$, the following test is applied

$$B_t(\Omega_s, \Omega_v, \nu_{MIR}, t, z_a, i_f, j_f) > \overline{B}_t(\nu_{MIR}, t, z_a, i_f, j_f) + C_{\Delta 3} + \breve{B}_t(\nu_{MIR}, t, z_a, i_f, j_f) \quad (44)$$

otherwise, the following test is applied

$$B_t(\Omega_s, \Omega_v, \nu_{MIR}, t, z_a, i_f, j_f) > \overline{B}_t(\nu_{MIR}, t, z_a, i_f, j_f) + C_{\Delta 3}\, \breve{B}_t(\Omega_s, \Omega_v, \nu_{MIR}, t, z_a, i_f, j_f) \quad (45)$$

When one of these tests failed, *i.e.*, the brightness temperature of a potential fire pixel is not sufficiently above the background temperate, the status flag is set to `BCKNOT`. If all three tests are successful, the pixel receives the `FRP` status flag value and the FRP [MW] for the slot t is estimated with

$$R_P(t, z_0, i_f, j_f) = \frac{\pi\, C_s\, \sigma_{SB}}{C_a(\nu_{MIR})} \frac{A_s(i_f, j_f)}{\Lambda'_a(\mu_v, \nu_{MIR}, U_{H_2O})} \Big(\widetilde{I}(\Omega_s, \Omega_v, \nu_{MIR}, t, z_a, i_f, j_f)\, \Gamma_{b1.5} - \overline{\widetilde{I}}_b(\nu_{MIR}, t, z_a, i_f, j_f)\Big). \quad (46)$$

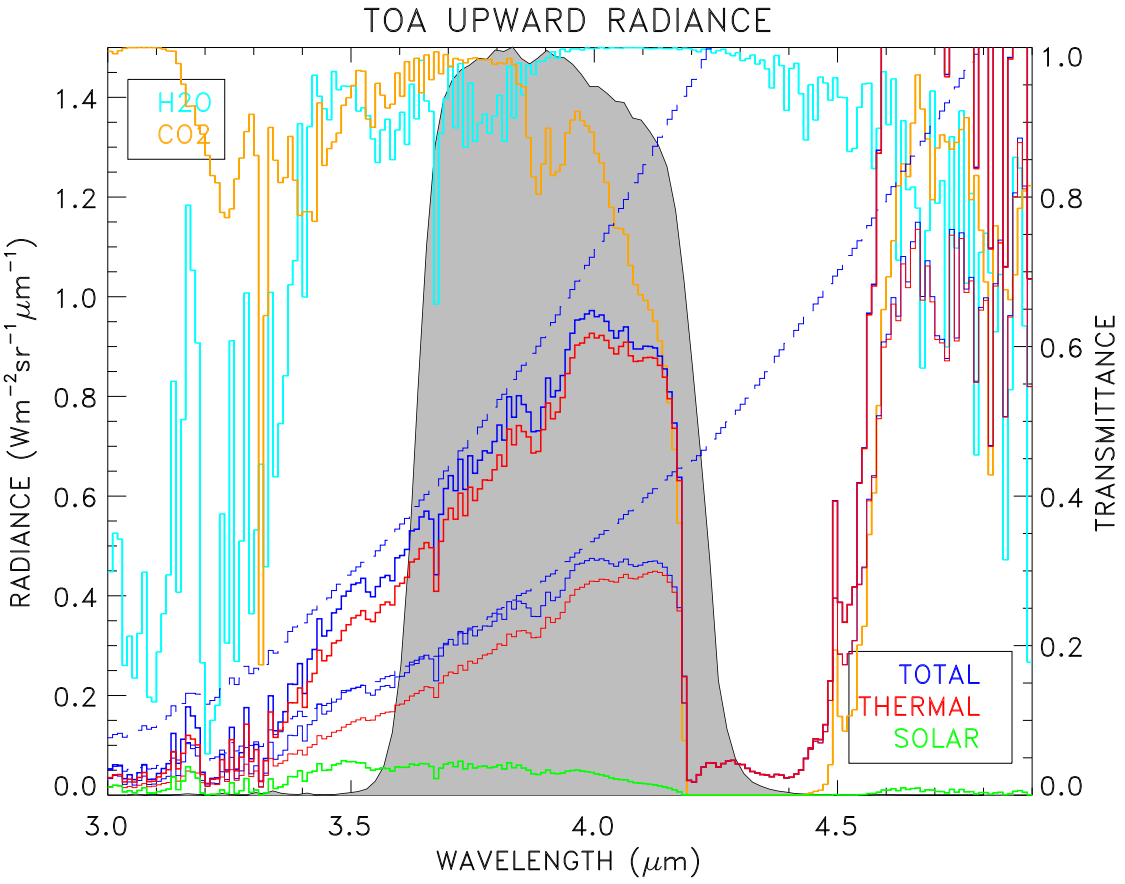

Figure 1: Spectral radiance and transmittance within the SEVIRI MIR band, shown in shaded grey, for two different surface temperatures of 290K and 310K. The solid (dashed) blue line is the spectral radiance at the TOA (surface) for these two tempratures. The themral and solar contributions are shown in red and green respectively. The H_2O and CO_2 transmittance are shown with the blue and brown lines.

where

$$A_s(i_f, j_f) = A_0/\mu_{v_0} \tag{47}$$

is the pixel area, C_s a scaling constant and $\Gamma_{b1.5}$ accounts for bias resulting from the resampling of the Level 1.0 images for the generation of Level 1.5 images. Note that this correction is only applied to the fired pixels, where the elevated radiance in a single pixel is actually dissipated in the neighbouring pixels during the resampling. Such dissipation is not applied on the background pixels. In this latter equation, the satellite viewing angle is computed with respect to the rectification grid nominal position.

When the radiance $\widetilde{I}(\Omega_s, \Omega_v, \nu_{MIR}, t, z_a, i_f, j_f)$ measured by SEVIRI saturates over a fire pixel, the corresponding pixel is assigned the `FRP_SAT` status flag value. The radiance is $\widetilde{I}(\Omega_s, \Omega_v, \nu_{MIR}, t, z_a, i_f, j_f)$ is substituted with the value $\widetilde{I}_s(\Omega_v, \nu_{MIR}, t, z_a)$ which represents typical radiance values that would have been observed if SEVIRI would not be subject to saturation (EUMETSAT 2008).

Because of the spectral width of the SEVIRI MIR band (Figure 1), the atmospheric correction of the FRP could not simply be performed taking into account the atmospheric transmittance Λ_a as indicated in Equation (16). Strictly speaking, the atmospheric transmittance Λ_a should be estimated with $\Lambda_a = \int_\nu I_f(\nu, z_a)/I_f(\nu, z_0)\, d\nu$. As the spectral behaviour of I_f is unknown, this quantity has to be treated as a "monochromatic" value. Since $\int_\nu (I_f(\nu, z_a)/I_f(\nu, z_0))\, d\nu \neq \int_\nu I_f(\nu, z_a)\, d\nu / \int_\nu I_f(\nu, z_0)\, d\nu$ and

the spectral variations of I_f pretty large in the MIR band, a "pseudo" transmittance Λ'_a is estimated to perform the atmospheric correction. This pseudo transmittance ${\Lambda_a}'(\mu_v, \nu_{MIR}, U_{H_2O})$ is estimated as the ratio between the radiance difference at level z_a and z_0

$$ {\Lambda'}_a(\mu_v, \nu_{MIR}, U_{H_2O}) = \frac{\widetilde{I}(\Omega_s, \Omega_v, \nu_{MIR}, t, z_a, i_f, j_f) - \overline{\widetilde{I}}_b(\nu_{MIR}, t, z_a, i_f, j_f)}{\widetilde{I}(\Omega_s, \Omega_v, \nu_{MIR}, t, z_0, i_f, j_f) - \overline{\widetilde{I}}_b(\nu_{MIR}, t, z_0, i_f, j_f)} \tag{48} $$

Values of ${\Lambda'}_a(\mu_v, \nu_{MIR}, U_{H_2O})$ have been pre-computed as a function of the total column water vapour U_{H_2O}. For each U_{H_2O} value, the mean transmittance has been estimated varying the CO_2 concentration between 330 and 380 ppmv, the aerosol optical thickness between 0.2 and 1.0 for various aerosol types, different atmospheric vertical profiles and surface brightness temperatures. The ozone concentration was set to 354 DU. The transmittance ${\Lambda_a}'(\mu_v, \nu_{MIR}, U_{H_2O})$ estimated with Equation (48) does not exactly follow an $\exp(-\tau_a(\nu_{MIR}, U_{H_2O}) \,/\, \mu_v)$ low. Instead, the following expression is used to express the transmittance changes as a function of the viewing angle θ_v

$$ {\Lambda'}_a(\mu_v, \nu_{MIR}, U_{H_2O}) = \exp\left(\frac{-\tau_a(\nu_{MIR}, U_{H_2O})}{\cos(A(\nu_{MIR}, U_{H_2O}) + B(\nu_{MIR}, U_{H_2O})\, q\, \theta_v + C(\nu_{MIR}, U_{H_2O})\, (q\, \theta_v)^2)}\right) \tag{49} $$

with $q = \pi/180$. Values of A, B and C have been adjusted to fit exactly the variations of $\Lambda_a(\mu_v, \nu_{MIR}, U_{H_2O})$ estimated with Equation (48) as a function of θ_v. These tabulated values are given in Section (A.2.1). The transmittance is linearly interpolated from this LUT according to the actual water vapour concentration U_{H_2O}.

3.7 FRP random error estimation

The estimation of R_P in Equation (46) is subject to random errors resulting from uncertainties in the estimation of C_a, Λ'_a, $\widetilde{I}$ and $\overline{\widetilde{I}}_b$. Assuming that these uncertainties are not correlated, the corresponding error σ_{R_P} is given by

$$ \sigma_{R_P}(t, z_0, i_f, j_f) = \sqrt{\sum_k \left(\frac{\partial R_P}{\partial k}\right)^2 \sigma_k^2} \tag{50} $$

where k represents the C_a, Λ'_a, $\widetilde{I}$ and $\overline{\widetilde{I}}_b$ variables. Solving the partial derivatives in Equation (50) leads to

$$ \sigma_{R_P} = R_P \sqrt{\left(\frac{\sigma_{C_a}}{C_a}\right)^2 + \left(\frac{\sigma_{\Lambda'_a}}{\Lambda'_a}\right)^2 + \left(\frac{\sigma_{\widetilde{I}}}{\widetilde{I}\,\Gamma_{b1.5} - \overline{\widetilde{I}}_b}\right)^2 + \left(\frac{\sigma_{\overline{\widetilde{I}}_b}}{\widetilde{I}\,\Gamma_{b1.5} - \overline{\widetilde{I}}_b}\right)^2} \tag{51} $$

These errors are taking the following values:

σ_{C_a} is the absolute error resulting from the spectral extrapolation of R_P. Assuming a fire temperature range of 675 to 1300K, the error σ_{C_a}/C_a is about 10% at one sigma.

$\sigma_{\Lambda'_a}$ is the total atmospheric correction absolute error resulting from (*i*) (σ_b): the uncertainty on the actual atmospheric vertical composition except the water vapour concentration and (*ii*) (σ_{H_2O}): the atmospheric correction error resulting from the uncertainty on the water vapour concentration ($\sigma_{U_{H_2O}}$). This total error writes

$$ \sigma_{\Lambda'_a} = \sqrt{\sigma_b^2 + \sigma_{H_2O}^2}. \tag{52} $$

The former error write

$$\sigma_b(\theta_v, \nu_{MIR}) = 10^{-5}\,\Lambda'_a(\mu_v, \nu_{MIR}, U_{H_2O}) \\ (710.51117 - 8.37751\,\theta_v + 0.92238\,\theta_v^2 - 0.02525\,\theta_v^3 + 0.00027\,\theta_v^4) \quad (53)$$

and the latter

$$\sigma_{H_2O} = \frac{\partial \Lambda'_a(\mu_v, \nu_{MIR}, U_{H_2O})}{\partial U_{H_2O}}\,\sigma_{U_{H_2O}} \quad (54)$$

with

$$\sigma_{U_{H_2O}} = 0.24287 + 0.11172\,U_{H_2O} - 0.00090\,U_{H_2O}^2 \quad (55)$$

Equation (55) holds for the total column water vapour field delivered by ECMWF.

$\sigma_{\widetilde{I}}$ represent the absolute radiometric error resulting from the combination of: (*i*) the radiometric noise (σ_n) of the SEVIRI MIR channel, (*ii*) the random errors ($\epsilon_{b1.5}$) related to the Level 1.5 processing effects and finally (*iii*) the instrument saturation above 335K. For this latter effect, the error term ($\sigma_{\widetilde{I}_s}$) corresponds to the uncertainty on the estimation of the radiance $\widetilde{I}_s$ that would have been observed if SEVIRI were not subject to saturation. Systematic errors such as calibration uncertainty are not included in this term. This error writes

$$\sigma_{\widetilde{I}} = \sqrt{\left(\sigma_n\right)^2 + \left(\widetilde{I}\,\epsilon_{b1.5}\right)^2 + \left(\sigma_{\widetilde{I}_s}\right)^2}\,. \quad (56)$$

Schmetz et al. 2002 report the radiometric performance of SEVIRI, against the error requirement specifications. The performance values reported are "end of life" predictions, based upon initial performance of the instrument and predicted in flight degradation to the end of the operational deployment of the instrument. At a specified signal equivalent to a 300 K brightness temperature, radiometric noise in the MIR channel is predicted to be 0.17 K, around half the specified 0.35 K error requirement for the mission. This translates to a radiometric noise of 0.038 $\mathrm{mWm^{-2}sr^{-1}(cm^{-1})^{-1}}$. Since detected fires typically correspond to radiance in the range 1 – 3.5 $\mathrm{mWm^{-2}sr^{-1}(cm^{-1})^{-1}}$, this corresponds into a relative error of about 1 – 4%. As the radiometric noise term is smaller than the other ones, it is currently neglected.

$\epsilon_{b1.5}$ represents the fractional uncertainty induced by the Level 1.5 processing chain (EUMETSAT 2008). The value of this parameter is given in Annex (C).

$\sigma_{\widetilde{I}_s}$ is the error associated with the saturated pixel default radiance value $\widetilde{I}_s(\Omega_v, \nu_{MIR}, t, z_a)$. This term is estimated only over saturated pixel. The value of this parameter is given in Annex (C).

$\sigma_{\widetilde{\overline{I}}_b}$ is the atmospherically corrected standard deviation of the background radiance $\widetilde{\overline{I}}_b(\nu_{MIR}, t, z_a, i_f, j_f)$.

3.8 FRP quality flag assessment

For those pixels for which the FRP has been successfully derived *i.e.*, that are assigned the `FRP` or `FRP_SAT` status flag value, a measure of detection confidence is derived based on the "average" characteristics of an active fire pixel. The average characteristics have been derived through analysis of the data. The tests attempt to relate the characteristics of the "potential" fire pixel to those of low and high intensity fire pixels. This measure is quite subjective since setting the limits of the comparison quite low would give all the detected fire pixels a high confidence and vice versa. The value of the output

confidence between 0 (no confidence) and 1(high confidence). This approach is based on the MODIS fire product confidence although the constraints have been adapted based on inspection of the SEVIRI data (Giglio et al. 2003). The thresholds (constraints) vary with solar zenith limits.

The confidence of a fire pixel is made up from 5 sub-confidence values which are defined using a ramp function :

$$S(x,\alpha,\beta)\begin{cases} 0 & : \quad x \leq \alpha \\ \frac{x-\alpha}{\beta-\alpha} & : \quad \alpha < x < \beta \\ 1 & : \quad x \geq \beta \end{cases} \tag{57}$$

These function are

$$\gamma_1 = S(B_t(\nu_{MIR}, i_f, t_f), \Gamma_{\gamma 11}, \Gamma_{\gamma 12}) \tag{58}$$
$$\gamma_2 = \min(S(z_4, , \Gamma_{\gamma 21}, \Gamma_{\gamma 22}),\ 1) \tag{59}$$
$$\gamma_3 = \min(S(z_\Delta, \Gamma_{\gamma 31}, \Gamma_{\gamma 32}),\ 1) \tag{60}$$
$$\gamma_4 = 1 - S(N_c, 0, N_s/2) \tag{61}$$
$$\gamma_5 = 1 - S(N_w, 0, N_s/2) \tag{62}$$
$$\tag{63}$$

where z_4 and z_Δ represent absolute deviations of the λ_{MIR} band and Δ_B, *i.e.*,

$$z_4(t, i_f, j_f) = \frac{B_t(\nu_{MIR}, t, z_a, i_f, j_f) - \overline{B}_t(\nu_{MIR}, t, z_a, i_f, j_f)}{\breve{B}_t(\nu_{MIR}, z_a, i_f, j_f)} \tag{64}$$

$$z_\Delta(t, i_f, j_f) = \frac{\Delta_B(t, i_f, j_f) - \overline{\Delta}_{Bb}(z_a, i_f, j_f)}{\breve{\Delta}_{Bb}(t, i_f, j_f)} \tag{65}$$

Note that when

$$B_t(\nu_{MIR}, i_f, t_f) > \Gamma_b \quad : \quad \gamma_1 = 1 \tag{66}$$
$$N_c \geq N_s/2 \quad : \quad \gamma_4 = 0 \tag{67}$$
$$N_w > N_s/2 \quad : \quad \gamma_5 = 0 \tag{68}$$

The overall confidence writes

$$\gamma = (\gamma_1\ \gamma_2\ \gamma_3\ \gamma_4\ \gamma_5)^{\frac{1}{5}} \tag{69}$$

and varies between 0 (no confidence) to 1 (high confidence). This quality flag is not estimated for pixels for which it has not been possible to derive the FRP, whatever the reason.

3.9 FRP Gridded estimation

3.9.1 Motivation for a correction for small fires

The rather coarse spatial resolution of SEVIRI presents a limitation with regard to estimating the total FRP emitted from all fires burning across the landscape. This is because the minimum FRP that a fire must emit to be detectable is inversely related to the pixel area. For example, an active fire necessarily occupies a smaller fraction of a SEVIRI pixel compared to that of a MODIS pixel due to the coarser spatial resolution achieved from geostationary orbit than from a near-polar orbit. Below a certain threshold, likely to be between 10^3 and 10^4 of a SEVIRI pixel, depending on fire temperature, solar radiant

contribution, background characterization, etc, the sub-pixel fractional area occupied by a fire will be too low to significantly elevate the radiance of the target pixel above the background. This results in an error of omission (*i.e.*, a true fire on the ground fails to be detected), and this process can be repeated across a landscape, meaning that SEVIRI can fail to detect a proportion of the smaller/less intense fires that higher spatial resolution sensors, such as MODIS are able to quantify.

The FRP Gridded algorithm addresses this low resolution bias and provides, as far as possible, an improved estimate of the FRP emitted across the landscape. Here fire pixels are accumulated in both the temporal and spatial domains, and an adjustment factor is applied to the FRP measured by SEVIRI. The aim of the adjustment factor is to account for the undetected FRP emitted by small fires as well as the FRP omitted as a result of the occasional saturation in the SEVIRI 3.9μm channel. Since there is no theoretical estimate of the "true" FRP emitted from open biomass burning, it is only possible to adjust the FRP-GRID product to agree with the FRP that would have otherwise been measured by an instrument with (*i*) a higher spatial resolution, and (*ii*) a greater dynamic range. The MODIS instrument satisfies these criteria.

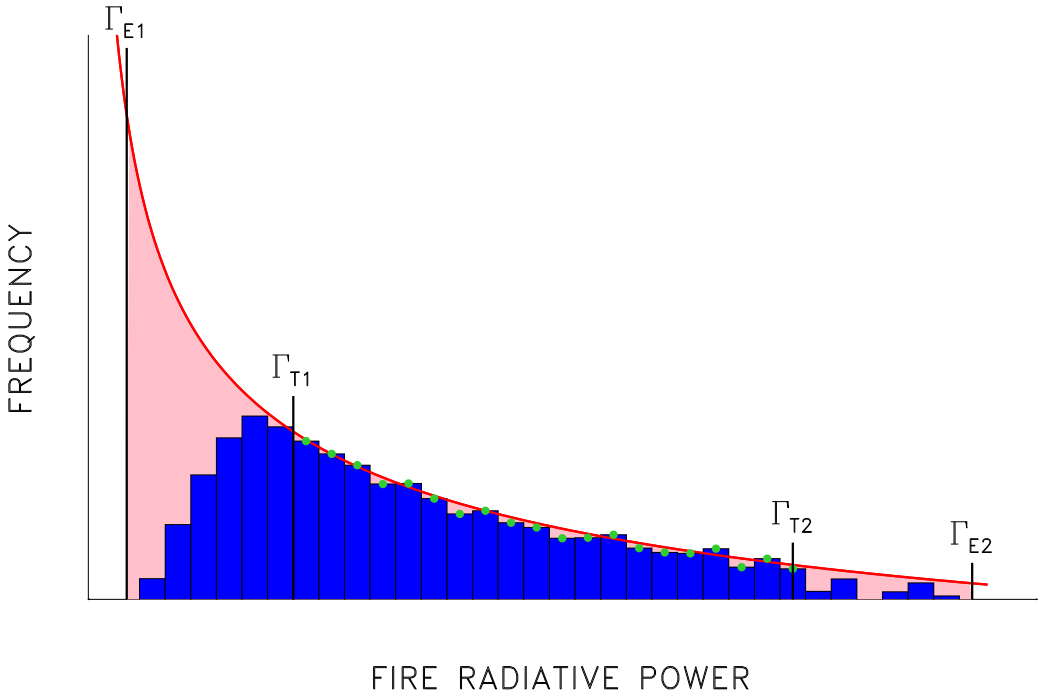

Figure 2: Schematic representation of a typical magnitude-frequency distribution $\mathcal{H}$ of FRP values (blue histogram). The theoretical distribution $\mathcal{F}$ is shown in red.

Roberts et al. (2005) show that when fire pixels are aggregated over a large geographic area and a period of several days the frequency-magnitude distribution $\mathcal{H}$ of FRP values derived from SEVIRI observations tends to follow a positively-skewed distribution. Here the frequencies decrease rapidly for FRP values smaller than $\approx$50 MW as a result of the effect described above (*i.e.*, due to the coarse SEVIRI spatial resolution and the consequent non-detection of low FRP pixels). Such a distribution is schematized with the blue histogram included in Figure (2). This frequency-magnitude distribution exhibits three differently structured regions. Between Γ_{T1} and Γ_{T2}, the distribution of FRP behaves as a power function, *i.e.*, there are more low-intensity fire pixels observed than large ones. For fire pixels with an associated FRP smaller than Γ_{T1}, the distribution shows a rapid decrease resulting from the low

spatial resolution of SEVIRI. Finally, above Γ_{T1}, the SEVIRI distribution suffers more from right hand truncation than MODIS due to a relatively lower saturation limit of 350K for SEVIRI compared to 500K for the MODIS low gain MIR channel.

The frequency-magnitude distribution $\mathcal{H}$ also changes in space and time as a function of land cover, land use practices, and fire processes that typically exhibit strong diurnal variations. Freeborn et al. (2009) demonstrate that SEVIRI-to-MODIS ratios of FRP are greater during the daytime than at night due to the increased prevalence and greater radiant contribution of the higher FRP fire pixels that typically occur during the day. Furthermore, fluctuations in the diurnal cycles of fire activity throughout the year also induce seasonal trends in the adjustment factors. Since seasonal trends in fire activity are directly coupled to the migration of biomass burning towards climatically favourable regions, the adjustment factor also exhibits spatial variability.

Although a near real-time adjustment is potentially the most attractive and adaptable approach, this would require the simultaneous processing of both the incoming SEVIRI and MODIS fire products. Such a method is thus contingent upon the availability of the MODIS fire product, which as of yet is not specified as "operational". To provide a self-reliant, stand alone FRP-GRID Product algorithm using only the SEVIRI data stream, therefore, requires the derivation of an adjustment factor from some form of training dataset. Here, concurrent and collocated fire pixels detected by SEVIRI and MODIS over 12 months between May 2008 and May 2009 were used to construct such a training dataset.

From relationships within the training dataset, a set of dynamic adjustment factors were developed based upon the strength of the SEVIRI fire signal. The FRP estimated by SEVIRI was related to the FRP estimated by MODIS via a power law function:

$$\int_{\Gamma_{E1}}^{\Gamma_{E2}} \mathcal{F}\, dR = \alpha \left(\int_{\Gamma_{E1}}^{\Gamma_{E2}} \mathcal{H}\, dR \right)^{\beta} \tag{70}$$

where $\mathcal{F}$ is the theoretical distribution that would have been observed with the higher spatial resolution MODIS instrument, and α and β are power law parameters that are unique for each of the four LSA SAF regions (EUMETSAT 2009). Whereas the integral on the left-hand side of Equation (70) represents the total FRP that would have been observed with MODIS, the integral on the right-hand side is the total FRP estimated from SEVIRI observations. Thus the power-law parameters are used to convert SEVIRI estimates of FRP into values that would have been observed by MODIS. In particular the exponent β is intended to utilize fluctuations in the SEVIRI observations of FRP in an effort to capture the spatio-temporal variability in the SEVIRI-to-MODIS ratios of FRP.

The power-law parameters α and β were derived for each of the four LSA SAF regions using the aforementioned training dataset. Although α and β were optimized to provide an unbiased estimate of the FRP that would be measured by MODIS over a 5° grid cell and at an hourly temporal resolution, it was found that the power law model could not deliver a prediction that was statistically different than that produced using a simple linear model with $\beta = 1.0$. Therefore the exponent β was universally fixed at 1.0, and α was retrieved for each of the four LSA SAF regions (EUMETSAT 2009). Furthermore it was found that the coefficient α derived for Europe (*i.e.*, Euro) was not statistically different than that derived for northern Africa (*i.e.*, NAfr); therefore the parameter in Europe was assigned the same value as northern Africa.

3.9.2 Corrected FRP Gridded concept

The FRP-GRID product is generated on a regular lat/lon grid at regular temporal interval. To this end, the FRP values $\widetilde{R}_P(t, i_f, j_f)$ derived for the image acquired at time t are summed over a regular grid of

resolution $G^\circ \times G^\circ$ grid box. For each grid point (x_G, y_G), the total FRP is

$$\widetilde{R}_P(t, i_G, j_G) = \sum_{(i_f, j_f) \in G^\circ \times G^\circ} \widetilde{R}_P(t, i_f, j_f) \tag{71}$$

This summation is performed over all the $\widetilde{R}_P(t, i_f, j_f)$ values in the grid box $G^\circ \times G^\circ$.

It is assumed that fire affected pixels are uniformly distributed within that area, so that FRP values derived over cloud free pixels are statistically also valid for cloudy pixels. Hence, the following value is also estimated

$$\widetilde{R}_{P\,f_s}(t, i_G, j_G) = \frac{1}{f_s(t, i_G, j_G)} \sum_{(i_f, j_f) \in G^\circ \times G^\circ} \widetilde{R}_P(t, i_f, j_f) \tag{72}$$

where $f_s(t, i_G, j_G)$ is the fraction of clear sky pixels over land within the $G^\circ \times G^\circ$ grid box. Similarly, when a grid box is too cloudy, *i.e.*, when $f_s < \Gamma_s$, Equation (72) is not estimated.

The gridded FRP, $\widetilde{R}_P(t, i_G, j_G)$ is temporally averaged over the period C_t to provide the FRP Gridded over the (i_G, j_G) grid box. During this temporal averaging process, a correction is applied to account for low intensity fires that have not been detected by SEVIRI. The estimation of FRPGrid value writes

$$\widehat{\widetilde{R}}_P(t_e, i_G, j_G) = \alpha_c(ROI) \left(\frac{1}{N_t} \sum_{t=t_e - C_t}^{t_e} \widetilde{R}_P(t, i_G, j_G) \right)^{\beta_c(ROI)} \tag{73}$$

where N_t is the number of avaialble FRPPixel products in the interval $[t_e - C_t, t_e]$. Thus, only values of $\widetilde{R}_P(t, i_G, j_G)$ are used in the sum. The estimation of $\alpha_c(ROI)$ and $\beta_c(ROI)$ are described in Section (3.9.1 and A.2.2). These coefficients are taking different values in the various ROIs. The cloud-corrected FRPGrid value $\widehat{\widetilde{R}}_{P\,f_s}(t_e, i_G, j_G)$ is estimatd in a similar way. The correction factor for the cloud is estimated with

$$C_c = \frac{\widehat{\widetilde{R}}_{P\,f_s}(t_e, i_G, j_G)}{\widehat{\widetilde{R}}_P(t_e, i_G, j_G)} \tag{74}$$

3.9.3 FRP-GRID error estimation

$\widehat{\widetilde{R}}_P(t_e, i_G, j_G)$ is the reference FRP-GRID product and therefore the error is estimated for that value.

Assuming that all the terms of Equation (73) are not correlated, the correspong error writes (omitting the (i_G, j_G) index)

$$\sigma_{\widehat{\widetilde{R}}_P}(t_e, i_G, j_G) = \sqrt{\sum_{k=1}^{n_k} \left(\frac{\partial \widehat{\widetilde{R}}_P}{\partial k}\, \sigma_k \right)^2} \tag{75}$$

where k represents the parameters $\alpha_c(ROI)$, $\beta_c(ROI)$ and $\widetilde{R}_P(t_i, i_G, j_G)$ in Equation (73). These error terms are taking the following values:

k = α_c

$$\left(\frac{\partial \widehat{\widetilde{R}}_P}{\partial \alpha_c} \right) \sigma_{\alpha_c} = \widehat{\widetilde{R}}_P\, \frac{\sigma_{\alpha_c}}{\alpha_c} \tag{76}$$

where σ_{α_c} comes from the uncertainty in the power law prediction linking MODIS and SEVIRI FRP values (see Section 3.9.1 and A.2.2).

$k = \beta_c$

$$\left(\frac{\partial \widehat{\widetilde{R}}_P}{\partial \beta_c}\right) \sigma_{\beta_c} = \widehat{\widetilde{R}}_P \ \ln\left(\frac{1}{N_t} \ \left(\sum_{t=t_e-C_t}^{t_e} \widetilde{R}_P(t)\right)\right) \ \sigma_{\beta_c} \tag{77}$$

where σ_{β_c} comes from the uncertainty in the power law prediction linking MODIS and SEVIRI FRP values (see Section 3.9.1 and A.2.2).

$k = \widetilde{R}_P(t_i)$

$$\sum_{t_i=t_e-C_t}^{t_e} \left(\frac{\partial \widehat{\widetilde{R}}_P}{\partial \widetilde{R}_P(t_i)}\right) \sigma_{\widetilde{R}_P(t_i)} = \frac{\widehat{\widetilde{R}}_P \ \beta_c \ \sqrt{\sum_{t_i=t_e-C_t}^{t_e} \sigma^2_{\widetilde{R}_P(t_i)}}}{\sum_{t_i=t_e-C_t}^{t_e} \widetilde{R}_P(t_i)} \tag{78}$$

where $\sigma_{\widetilde{R}_P(t_i)}$ is equal to

$$\sigma_{\widetilde{R}_P(t_i)} = \sqrt{\sum_{(i_f,j_f)\in G^\circ \times G^\circ} \left(\sigma_{\widetilde{R}_P(t_i,i_f,j_f)}\right)^2} \tag{79}$$

where $\sigma_{\widetilde{R}_P(t_i,i_f,j_f)}$ is given by Equation (50).

4 ASSUMPTIONS AND LIMITATIONS

4.1 FRP-PIXEL algorithm assumptions

The FRP algorithm relies on the following main assumptions:

Assumption	Eq.	Consequence
The fire and background emission are isotropic.	3	The inaccuracy resulting from this assumption is probably larger for the background than for the fire area, but the actual effect still needs been quantified.
The Planck's radiation law is well approximated by a fourth order power law in the 3.4–4.2μm interval.	10	This assumption introduces a $\pm$12% relative error in the FRP estimation for fires lying within temperature range 665 – 1365 k (Wooster et al. 2005, Fig. 2).
The fire emissivity does not change with wavelength.	12	To be evaluated.
The effects of aerosols and trace gases are not taken into account.	14	The aerosol optical thickness in the MIR band is typically lower than 0.05 which translates into a transmittance larger than 0.95. The uncertainty on the atmospheric transmittance for a given water vapour concentration ranges between 1 and 2% according to the viewing angle.
The fire emission is equal to one.	14	The burning area is very small compared to the pixel size so that its contribution can be neglected.
The pixel fire fraction can be neglected.	15	The atmospheric radiance is not affected by the presence of a fire and the atmospheric contribution is assumed to originate only from the background.
	16	The approximations made in Equations (15) and (16) to derive Equation (18) from Equation (13) are estimated to about introduce a $\pm$12% maximum relative error (Wooster et al. 2005, Fig. 4). Inaccuracies in the characterisation of the background will have a greater effect as the fire temperature decreases.
Because of the spectral width of the SEVIRI MIR band (Figure 1), the atmospheric correction of the FRP could not simply be performed taking into account the atmospheric transmittance Λ_a as indicated in Equation (16).	16	A concept a pseudo transmittance has been used instead to perform the atmospheric correction on the difference between the fire pixel and the background radiances described in Equation (48).
The background radiance is determined from the clear sky surrounding pixels not affected by fires.	37	Inaccuracies in the characterisation of the "true" background radiance increase as the fire size and temperature decrease (Wooster et al. 2005, Fig. 2).
It is assumed that fire affected pixels are uniformly distributed within a grid cell, so that the value derived over cloud free pixels is also valid for the cloudy part of the grid box.	72	To be evaluated

4.2 FRP-PIXEL algorithm limitations

In addition to the assumption effects listed in Section (**??**), the FRP algorithm is subject to other sources of uncertainties essentially due to the characteristics of SEVIRI and associated image level 1.5 processing. Among these limitations, one can site:

- The spatial resolution of SEVIRI represents clearly a major limitation to an accurate FRP estimation. The most significant consequence of this low spatial resolution is the non-detection of smaller/less intense fires that MODIS can detect for instance but SEVIRI misses. Consequently, FRP values derived from SEVIRI underestimates by about 40% those derived from MODIS observations (Roberts et al. 2005).
- The non-linearity of the SEVIRI 3.9 channel above 310K and the saturation of that band above 335K are responsible for error in the FRP estimation (Lattanzio and Govaerts 2006).
- The FRP derived value is quite sensitivity of the fire location within the pixel. This effect is due to the shape of the point spread function, ie, its departure from an ideal square box. A fire located at the centre of the instrument instantaneous field-of-view will elevate the pixel temperature much more than a fire located fare away from its centre. Additionally, abnormally low radiances might be observed surrounding a fire pixel due to the negative lobes of the point spread function. As a result, the background temperature might be colder, increasing thereby the estimated FRP value (EUMETSAT 2008).
- Finally, the generation of the SEVIRI level 1.5 images, in particular the re-projection on a standard grid, tends to smooth high radiance values resulting from fires (EUMETSAT 2008). The coefficient $\Gamma_{b1.5}$ in Equation (46) accounts for this effects. For the time being, the exact value of this coefficient still remains to be evaluated.

4.3 Assumptions and limitations of the FRP Gridded algorithm

The FRP Gridded algorithm was designed to spatially and temporally accumulate individual fire pixels; therefore the assumptions and limitations of the pixel-level FRP algorithm (see Sections **??** and **??**) are inherently included in this higher-level algorithm. The assumptions and limitations specifically associated with the FRP Gridded algorithm are presented here:

- The parameters implemented in the FRP Gridded algorithm were derived from a training dataset of concurrent and collocated fire pixels detected by SEVIRI and MODIS. The sensor-to-sensor relationships contained within the training dataset are representative of the observations of fire activity at the times of the MODIS overpasses, typically centred around 1:30, 10:30, 13:30, and 22:30 local time (so at four regularly spaced points over the full diurnal cycle). Therefore, during the development of the FRP Gridded algorithm, it was assumed that relationships between SEVIRI and MODIS at the times of the MODIS overpasses could be extended to characterize sensor-to-sensor relationships at other times in the local diurnal cycle of fire behaviour. Furthermore, since active fire pixels in the training dataset were subset from the centre of the MODIS granule, the FRP Gridded algorithm attempts to reproduce the "optimum" thermal response of MODIS in the absence of image distortions that affect the edge of the MODIS scene.
- The FRP Gridded algorithm does not rely on any additional external data (*e.g.*, topography, vegetation type, canopy cover, *etc.*) or ephemeris data (*e.g.*, view zenith angle, ground sampling area,

etc.) to characterize the relationship between SEVIRI and MODIS observations of FRP. Instead the FRP Gridded algorithm simply assumes that the variability in the MODIS-derived estimates of FRP can be explained by the variability in the SEVIRI-derived estimates of FRP.

- An underlying power-law function was found at the continental scale between the FRP observed by SEVIRI and that observed by MODIS. However this power-law function could not be statistically distinguished from a simple linear regression at the regional scale. Therefore it could only be assumed that SEVIRI-derived estimates of FRP were directly proportional to MODIS-derived estimates. Such a simple linear regression only captures the macroscopic features of the sensor-to-sensor relationships and does not account for any temporal variability that is induced by diurnal or seasonal cycles of fire activity. By deriving different regression coefficients for each of the four LSA SAF regions, however, the FRP Gridded algorithm does incorporate broad spatial differences in the sensor-to-sensor relationships that potentially arise from (*i*) differences in fire regimes, and (*ii*) differences in SEVIRI view angles.

- During the development of the FRP Gridded algorithm, the hourly-average of FRP estimated by SEVIRI was binned, and the median values within each bin were related to MODIS observations of FRP. Furthermore a weighted least squares (WLS) routine was used to account for the increase in variance with an increase in FRP (see Equation 51). Finally, the intercept of the linear regression was forced through the origin. In combination, these techniques accounted for the relatively larger number of low FRP fire pixels and the greater uncertainty in the SEVIRI-to-MODIS ratios of FRP associated with the low FRP observations. Hence the FRP Gridded algorithm was developed to assuage any bias towards observations of intense (*i.e.*, high FRP) fire activity at the expense of (the significantly more common) low to moderate FRP activity.

- It was found that due to the positively-skewed distributions of FRP measured by each sensor (*e.g.*see Figure 2), the coefficient tends to underpredict the FRP that would have been measured by MODIS at coarser spatio-temporal resolutions. When applied at the spatio-temporal resolution of the gridded fire product, the coefficient is very good at predicting the median MODIS measurement of FRP. This strategy is desirable at 5° grid cell resolution and hourly temporal resolution since it ensures that, for any gridded prediction, 50% of the MODIS measurements of FRP will be above the "Gridded Product" prediction of FRP, while 50% will be below. For most observations, however, and in particular for observations of low fire activity, the FRP measured by MODIS is not normally distributed around the Gridded Product prediction. Instead the distribution of the FRP measured by MODIS is positively skewed towards higher values (again see Figure 2). Hence, the coefficient tends to underpredict the mean FRP measured by MODIS at 5° grid cell resolution and hourly temporal resolution. Ultimately then, when 5° grid cells are accumulated over time (and space), the Gridded Product algorithm will underpredict the sum of the FRP that would have been measured by MODIS since (as in the case of any positively skewed distribution) the sum of the median predictions will be less than the sum of the mean predictions. Furthermore, if no fires are detected by SEVIRI in a 5° grid cell, then no adjustments are made to the native SEVIRI observation. Quite often in South America and Europe, for example, MODIS detects a considerable amount of FRP whereas SEVIRI does not detect a single fire pixel due to the presence of only smaller fires and/or extreme viewing geometries. Therefore if the user is working with the Gridded Product to estimate total FRP at temporal resolutions of around one week or greater (*i.e.*, by accumulating values from many Gridded Product files), it is recommended that the user multiply the FRP values stored in the individual Gridded Product files by the weekly/regional validation coefficients (which can be found in the final column of the summary table presented in Appendix A.2.2) in order to provide an unbiased weekly estimate of the FRP that would have been measured by MODIS over the entire LSA SAF region had it had the temporal resolution of the original

Gridded Product files. The confidence in this regional, weekly temporal resolution prediction of FRP (expressed in terms of Pearson's correlation coefficient, R2) that the user can expect at is also shown in the final column of the summary table presented in Appendix A.2.2 The reliability of the weekly/regional coefficients when applied at other temporal/spatial resolutions has not been evaluated.

- The use of a 5° gridded domain at hourly temporal resolution was necessary to accumulate a sufficient number of fire pixels to (*i*) overwhelm the extreme variability in the SEVIRI-to-MODIS ratios observed for individual fire events, and (*ii*) increase the range of FRP over which the model relationship between SEVIRI and MODIS was developed. Grid cells between latitudes of $\pm 18°$ were at least 95% of the area of those centred on the equator; however grid cells centred on latitudes of $\pm 36°$ were 19% smaller by area than those centred on the equator. Since grid cells in the former belt contained the majority of fire pixels, latitudinal differences in the ground area enclosed within individual grid cells were not considered to significantly impact the development of the FRP Gridded algorithm. Furthermore, although the number of fire pixels detected in a 5° grid cell would theoretically decrease at higher latitudes due to a decrease in the ground sampling area (assuming observations of identical fire behaviour), this artefact was ignored since the latitudinal gradient existed in both the training and validation datasets.

- Whilst this work has strictly focused on a methodology to adjust a geostationary active fire product to account for the undetected presence of smaller and/or less intense fires, it is also true that MODIS itself is likely to miss a proportion of the most weakly burning events. Indeed the MODIS distributions of FRP also exhibit characteristics of left-hand truncation (*c.f.*, Figure 2). This feature of the frequency-magnitude distribution can be attributed to either (*i*) a self-imposed limit on the number of small and/or less intense fires that can potentially exist on the landscape, or (*ii*) the inability of the MODIS sensor and fire detection algorithm to distinguish a portion of the smallest and/or least intense fires from the non-fire background. In reality it is probably a mixture of the two, and thus it is expected that MODIS also suffers from some low-resolution bias, just that it is less severe than that of SEVIRI. Importantly therefore, it should be remembered that the FRP-GRID Product algorithm does not account for the energy emitted by landscape fires that would also remain undetected by MODIS, but rather adjusts the SEVIRI observations to attempt to replicate the magnitude of FRP that would have been measured if MODIS had observed the same fire activity at the same time as SEVIRI.

- In accordance with similar calculations (*e.g.*, Giglio et al. 2006), the cloud correction factor (see Equations 73 to 75) was developed under the assumption that the FRP emitted by landscape fires is uniformly distributed over a 5° grid cell. As such the cloud correction factor does not account for the potential reduced occurrence of landscape fires, or the potential reduced fire intensity and area, due to lower surface temperatures and increased relative humidity under cloud.

References

Andreae, M. O. (1991). Biomass burning: Its history, use and distribution, and its impact on environmental quality in global climate. In J. Levine (Ed.), *Global biomass burning: Atmosphere, climatic, and biospheric implications*, pp. 3–21. Cambridge, MA: MIT Press.

Derrien, M. and H. Le Gleau (2005). Msg/seviri cloud mask and type from safnwc. *International Journal of Remote Sensing 26*(21), 4707–4732.

Dozier, J. (1981). A method for satellite identification of surface temperature fields of sub-pixel resolution. *Remote Sens. Environ. 87*, 272–282.

EUMETSAT (2008). SAF for Land Surface Analysis: Validation Report FRP. Technical Report SAF/LAND/IM/VR FRP/I 08, EUMETSAT.

EUMETSAT (2009). Fire Radiative Power Product User Manual. Technical Report SAF/LAND/IM/PUM_FRP/1.1, EUMETSAT.

Freeborn, P. H., M. Wooster, B. Malamud, G. Roberts, and W. Xu (2009). Development of a virtual active fire product for africa through a synthesis of geostationary and polar orbiting satellite data. *Remote Sensing of Environment 113*, 1700–1711.

Giglio, L., I. Csiszar, and C. Justice (2006). Global distribution and seasonality of active fires as observed with the Terra and Aqua MODIS sensors. *Journal of Geophysical Research - Biogeosciences 111*(G02016), doi:10.1029/2005JG000142.

Giglio, L., J. Descloitres, C. O. Justice, and Y. J. Kaufman (2003). An enhanced contextural fire detection algorithm for MODIS. *Remote Sensing of Environment 87*, 273–282.

Govaerts, Y. (2006). RTMOM V0B.10 user's manual. Technical Report EUM/MET/DOC/06/0503, EUMETSAT.

Govaerts, Y., J. Pereira, B. Pinty, and B. Mota (2002). Impact of fires on surface albedo dynamics over the African continent. *Journal of Geophysical Research 107*(D22), doi:10.1029/2002JD002388.

Justice, C. O., L. Giglio, S. Korontzi, J. Owens, J. T. Morisette, D. Roy, J. Descloitres, S. Alleaume, F. Petitcolin, and Y. Kaufman (2002). The MODIS fire products. *Remote Sens. Environ. 83*, 244–262.

Kaufman, Y. J., R. G. Kleidman, and M. D. King (1998). SCAR-B fires in the tropics: Properties and remote sensing from EOS-MODIS. *Journal of Geophysical Research 103*, 31955–31968.

Kaufman, Y. J., L. Remer, R. Ottmar, D. Ward, L. Rong-R, R. Kleidman, R. Frase, L. Flynn, D. McDougal, and G. Shelton (1996). Relationship between remotely sensed fire intensity and rate of emission of smoke : SCAR-C experiment. In J. Levine (Ed.), *Global biomass burning*, pp. 685–696. MIT Press.

Kirkevag, A., T. Iverson, and A. Dahlback (1991). On radiative effects of black carbon and sulphate aerosols. *Atmos. Environ. 33*, 2661–2635.

Lattanzio, A. and Y. Govaerts (2006, December 2006). Report on the comparison of the fire thermal anomaly algorithm products generated with meteosat-8 and meteosat-9 data. Technical Report EUM/MET/REP/06/0483, EUMETSAT.

MeteoFrance (2007). Algorithm theoretical basis document for cloud products. Technical Report SAF/NWC/CDOP/MFL/SCI/ATBD/01, MeteoFrance.

Roberts, G., M. J. Wooster, G. L. W. Perry, N. Drake, L.-M. Rebelo, and F. Dipotso (2005). Retrieval of biomass combustion rates and totals from fire radiative power observations: Application to

southern Africa using geostationary SEVIRI imagery. *Journal of Geophysical Research 110*, 21111.

Schmetz, J., P. Pili, S. Tjemkes, D. Just, J. Kerkmann, S. Rota, and A. Ratier (2002). An introduction to meteosat second generation. *BAMS 83*(7), 977–992.

Scholes, R. J., J. Kendall, and C. O. Justice (1996). The quantity of biomass burned in southern africa. *Journal of Geophysical Research 101*, 23667–23676.

Schultz, M. (2002). On the use of atsr fire count data to estimate the seasonal and interannual variability of vegetation fire emissions. *Atmos. Chemistry and Physics 2*, 387–395.

Wooster, M. J. (2002). Small-scale experimental testing of fire radiative energy for quantifying mass combusted in natural vegetation fires. *Geophysical Research Letters 29*, 23–1.

Wooster, M. J., G. Roberts, G. L. W. Perry, and Y. J. Kaufman (2005). Retrieval of biomass combustion rates and totals from fire radiative power observations: FRP derivation and calibration relationships between biomass consumption and fire radiative energy release. *Journal of Geophysical Research 110*, 24311.

Wooster, M. J., Roberts, G., Freeborn, P. H., Xu, W., Govaerts, Y., Beeby, R., He, J., Lattanzio, A., Fisher, D., and Mullen, R. (2015). LSA SAF Meteosat FRP products Part 1: Algorithms, product contents, and analysis. *Atmospheric Chemistry and Physics 15*, 13217-13239, doi:10.5194/acp-15-13217-2015.

Wooster, M. J., B. Zhukov, and D. Oertel (2003). Fire radiative energy for quantitative study of biomass burning: derivation from the BIRD experimental satellite and comparison to MODIS fire products. *Remote Sens. Environ. 11*, 221–229.

Annex

A FRP INPUT INFORMATION

A.1 Dynamic input information

A.1.1 SEVIRI data

The FRP algorithm requires the following information from SEVIRI observations:

- SEVIRI band VIS0.6 (λ_{VIS}), IR3.9 (λ_{MIR}), IR10.8 (λ_{TIR1}) and IR12.0 (λ_{TIR2})
- SEVIRI actual SSP and acquisition time of each line

A.1.2 Ancillary data

The FRP requires a reliable cloud mask. The mask generated by the nowcasting SAF is used (MeteoFrance 2007).

A.2 Static input information

A.2.1 Atmospheric transmittance LUT

The following coefficients are used for the estimation of the atmospheric transmittance (Equation 49) of the SEVIRI λ_{MIR} band based on MODTRAN v5 simulations:

U_{H_2O}	τ_a	A	B	C
MSG1/SEVIRI λ_{MIR} band				
05	0.336124	0.030017368	0.81365422	0.074912042
10	0.345650	0.029765264	0.82138959	0.072212582
15	0.354402	0.029690540	0.82647446	0.070406239
20	0.362770	0.029800270	0.82993082	0.069430036
25	0.370988	0.029856317	0.83291153	0.068731294
30	0.379226	0.029742839	0.83616903	0.067856662
35	0.390364	0.029627315	0.84181733	0.066263967
40	0.403195	0.029444412	0.84863101	0.064211751
45	0.416773	0.029145209	0.85585032	0.061881701
50	0.426809	0.028949352	0.86003283	0.060420468
55	0.438261	0.028702154	0.86511544	0.058599510
60	0.447527	0.028514209	0.86842034	0.057325674
MSG2/SEVIRI λ_{MIR} band				
05	0.321467	0.027316134	0.85553159	0.053776369
10	0.330826	0.027146853	0.86218103	0.051529188
15	0.339444	0.027144522	0.86634780	0.050134439
20	0.347699	0.027296571	0.86903740	0.049501088
25	0.355823	0.027378935	0.87135218	0.049089632
30	0.363977	0.027320702	0.87392271	0.048510673
35	0.375047	0.027258106	0.87873549	0.047238299
40	0.387816	0.027118670	0.88465986	0.045519157
45	0.401340	0.026861487	0.89100152	0.043518266
50	0.411327	0.026705954	0.89455246	0.042319332
55	0.422738	0.026520877	0.89891372	0.040795479
60	0.431966	0.026366685	0.90168035	0.039760417
MSG3/SEVIRI λ_{MIR} band				
05	0.327308	0.028174669	0.84295359	0.060058842
10	0.336607	0.027987465	0.84984313	0.057728070
15	0.345172	0.027947670	0.85427913	0.056223291
20	0.353382	0.028096801	0.85717170	0.055505532
25	0.361462	0.028170605	0.85968094	0.055017009
30	0.369577	0.028105064	0.86244269	0.054361013
35	0.380605	0.028012276	0.86752909	0.052985499
40	0.393337	0.027858960	0.87372066	0.051169367
45	0.406825	0.027590711	0.88032620	0.049073224
50	0.416780	0.027413110	0.88408697	0.047793008
55	0.428159	0.027211082	0.88867247	0.046179670
60	0.437357	0.027046571	0.89161614	0.045069551

U_{H_2O}	τ_a	A	B	C
MSG4/SEVIRI λ_{MIR} band				
5.	0.304241	0.026362991	0.87447705	0.044716444
10	0.313859	0.026189109	0.88100757	0.042406204
15	0.322697	0.026199963	0.88488715	0.041078120
20	0.331145	0.026388030	0.88722163	0.040563213
25	0.339440	0.026491817	0.88919426	0.040276985
30	0.347750	0.026450220	0.89144541	0.039815194
35	0.358964	0.026398802	0.89591418	0.038661976
40	0.371863	0.026279247	0.90147256	0.037063944
45	0.385505	0.026032959	0.90745060	0.035189725
50	0.395598	0.025882605	0.91071019	0.034102771
55	0.407105	0.025709599	0.91475340	0.032702023
60	0.416420	0.025582324	0.91721792	0.031793639

These coefficients have been estimated with the MODTRAN v5.

A.2.2 Small fire correction LUT

The following coefficients are used for the small fire correction (Equation 73) :

LSA Region	**WLS param. estimates (with std. error)**				**Validation results at 5° and hourly resol.**		**Validation results at LSA region and weekly resol.**	
(Abbreviation)	α_c	(σ_{α_c})	β_c	σ_{β_c}	**Slope**	(R^2)	**Slope**	(R^2)
Northern Africa (NAfr)	1.674	(0.062)	1.0	(0.0)	1.04	(0.76)	1.15	(0.96)
Southern Africa (SAfr)	1.464	(0.062)	1.0	(0.0)	1.02	(0.91)	1.24	(0.96)
South America (SAme)	2.057	(0.224)	1.0	(0.0)	0.97	(0.34)	1.89	(0.83)
Europe (Euro)	1.674	(0.173)	1.0	(0.0)	1.72	(0.85)	4.94	(0.84)

A.2.3 Ancillary data

The FRP algorithm relies on the following static information:

- Geographical coordinates of the Land SAF regions.

B DESCRIPTION OF THE PRODUCT LIST

B.1 Near real-time FRP product

The FRP product is available at the pixel resolution for each processed slot, *i.e.*, every 15 min. A status flag is associated to each pixel. This flag contains information on the processing status of the pixel and the confidence of the retrieval in case a $R_P > 0$. The pixel processing status includes the following states:

Name	Equations	Description
NOTPOT	31	The pixel has no potential fire, *i.e.*, Eq. (31) is not satisfied.
FRP	46	The pixel has a valid FRP value
FRP_SAT		The pixel has a valid FRP value but the 3.9 channel saturated, *i.e.*, the BT exceeds 335K.
CLOUD	19 to 21	The pixel is not clear sky, no fire detection can take place
SUNG	26	The pixel is affected by sunglint, no fire detection can take place
SUNGRATIO	30	The pixel belong to $\mathcal{P}_3(t,i,j)$ defined by test (30)
NOBCK	33	It has not been possible to define the background temperature
BCKNOT		The difference between the potential fire pixel and the background is not significant
WATEREDGE	22	The pixel is affected by water body edges, no fire detection can take place
NOTPROC		The pixel is outside a ROI and has not been processed by FRP

The processing flag is available in the SEVIRI projection as a matrix. For each pixel with a valid FRP value, the following information is saved:

Name	Symbol	Equation	Description
		Time and location	
ACQTIME	t		Detection time (hour and minute)
LONGITUDE			Longitude of the pixel centre in degree
LATITUDE			Latitude of the pixel centre in degree
ABS_PIXEL	i_f		Column number in the SEVIRI native image
ABS_LINE	j_f		Line number in the SEVIRI native image
REL_PIXEL			Column number with respect to the local ROI
REL_LINE			Line number with respect to the local ROI
		Fire pixel	
PIXEL_SIZE	A_s	47	Pixel area in km^2
PIXEL_VZA	θ_v		Satellite viewing angle in degree
PIXEL_ATM_TRANS	Λ_a	49	Total atmospheric transmittance
FIRE_CONFIDENCE	γ	69	Quality flag
BT_MIR	$B_t(\nu_{MIR}, z_a)$		TOA BT in the λ_{MIR} band
BT_TIR1	$B_t(\nu_{TIR1}, z_a)$		TOA BT in the ν_{TIR1} band
RAD_PIX	$\widetilde{I}$		Radiance of a fire pixel
		Background	
BW_NUMPIX	N_b	33	Number of valid pixel in $\mathcal{B}$
BW_SIZE	s_b		Size of the background window
BBT_MIR	$\overline{B}_t(\nu_{MIR}, z_a)$	34	TOA mean background BT in the λ_{MIR} band
BW_BTD	$\overline{\Delta}_{Bb}(t, z_a)$	36	TOA diff. between λ_{MIR} and ν_{TIR1} bands.
RAD_BCK	$\widetilde{I}_b$		Mean radiance of the background window
SDT_BCK	$\sigma_{\widetilde{I}_b}$		Standard deviation of the background window
		FRP and Error	
FRP	$\widetilde{R}_P(t, i_f, j_f)$	46	Estimated fire radiative power
FRP_UNCERTAINTY	$\sigma_{\widetilde{R}_P}(t, i_f, j_f)$	50	Estimated fire radiative power error
ERR_FRP_COEFF	σ_{C_a}/C_a	51	Relative error on the FRP spectral extrapolation
ERR_ATM_TRANS	$\sigma_{\Lambda'_a}/\Lambda'_a$	51	Atmosphere pseudo-transmittance relative error
ERR_RADIOMETRIC	$\sigma_{\widetilde{I}}/(\widetilde{I}\,\Gamma_{b1.5} - \overline{\widetilde{I}}_b)$	51	Fire pixel radiance relative error
ERR_BACKGROUND	$\sigma_{\widetilde{I}_b}/(\widetilde{I}\,\Gamma_{b1.5} - \overline{\widetilde{I}}_b)$	51	Barckground radiance relative error.
ERR_VERT_COMP	σ_b	53	Absolute error on the atmospheric transmittance resulting from the uncertainty on the actual atmospheric vertical composition except the water vapour composition.

The format of the output files and the access to the FRP products are described in EUMETSAT (2009).

B.2 Gridded FRP product

The following information is saved for each grid point:

Name	Symbol	Equation	Description
GFRP	$\widehat{\widetilde{R}}_P$	73	Hourly gridded fire radiative power corrected for undected small fires.
GFRP_ERROR	$\sigma_{\widehat{\widetilde{R}}_P}$	75	Estimated error of $\widehat{\widetilde{R}}_P$
GFRP_ERR_FRP	†	78	Error contribution due to the error on the $\widetilde{R}_P(t_i)$ terms
GFRP_CLOUD_CORR	C_c	74	Factor to apply on $\widehat{\widetilde{R}}_P$ to perform the cloud correction
GFRP_RANGE			Difference between the Max and Min $\widetilde{R}_P(t, i_G, j_G)$
GRIDPIX			Number of pixels affected at least once by fires in a grid box
NUMIMG	N_t		is the number of avaialble FRPPixel products in the interval $[t_e - C_t, t_e]$
NUMFIRES			Average number of fires in the grid box during period C_t
BURNTSURF			Percentage of fire-affected pixel within the gridbox
ATMTRANS			Mean hourly Λ'_g value within the gridbox
GFRP_QI	??	??	Quality indicator associated with the estimation of $\widehat{\widetilde{R}}_P$
LATITUDE			Grid centre latitude value in degree
LONGITUDE			Grid centre longitude value in degree

$\dagger = \sum_{t=t_e-C_t}^{t_e} \frac{\beta_c \, \sigma_{\widetilde{R}_P(t_i)}}{\sum_{t=t_e-C_t}^{t_e} \widetilde{R}_P(t)}$

C FRP SETUP PARAMETERS

Symbol		Min	Max	Default	Definition
Clear sky pixel identification					
Γ_{01}	K			1.5	Threshold value for Eq. (19)
Γ_{02}				0.7	Threshold value for Eq. (20)
Γ_{03}	K			6.0	Threshold value for Eq. (21)
Γ_{04}	K			320	Threshold value for Eq. (22)
Potential fire identification					
C_{11}	K/degree			-0.3 / 0.0$^{(1)}$	Constant value (Eq. 23)
C_{12}	K			310.5 / 280.0$^{(1)}$	Constant value (Eq. 23)
C_{21}	K/degree			-0.0049 / 0.0$^{(1)}$	Constant value (Eq. 24)
C_{22}	K			1.75 /1.0$^{(1)}$	Constant value (Eq. 24)
C_{41}	K/degree			-0.012	Constant value (Eq. 28)
C_{42}	K			2.5	Constant value (Eq. 28)
Γ_{g1}	degree			0.0	Minimum threshold value for sunglint
Γ_{g2}	degree			5.0	Maximum threshold value for sunglint
Γ_{g3}	degree			2.0	Maximum threshold value for sunglint (background)
Γ_{VR}				0.7	MIR / VIS ratio threshold
Γ_{TRR}				0.0195	Threshold value for the MIR / TIR1 ratio
(1) Night time value, *i.e.*, when $\theta_s > 90$					
Background characterisation					
Γ_c				0.65	Min fraction of valid background pixel
Γ_D	K			10.0	Δ_B threshold value
Γ_F	K			330.0	Upper limit for the background window
Γ_{PSF}	K			270.0 / 0.0$^{(1)}$	PSF threshold value
(1) Night/twilight time value, *i.e.*, when $\theta_s > 70$					

FRP assessment					
$\widetilde{I_s}$	$mWm^{-2}sr^{-1}(cm^{-1})^{-1}$			4.08	Default radiance value assigned to saturated pixels
$\sigma_{\widetilde{I_s}}$	$mWm^{-2}sr^{-1}(cm^{-1})^{-1}$			0.49	Error associated to $\widetilde{I_s}$
C_a	$mWm^{-2}K^{-4}$			satellite dependent	Spectral extrapolation factor
$\Gamma_{b1.5}$				1.0	Bias resulting from the resampling of the Level1.0 images for the generation of Level 1.5 images. No bias correction is applied as it is shown to be region/time dependent.
$\epsilon_{b1.5}$				0.084	Uncertainty resulting from the Level 1.5 processing chain
$C_{\Delta 1}$	K			2.0	Constant value
$C_{\Delta 2}$	K			2.5	Constant value
$C_{\Delta 3}$	K			2.0	Constant value
$\Gamma_{\gamma 11}$	K			287.0 / 280.0(1)	Minimum threshold value
$\Gamma_{\gamma 12}$	K			327.0 / 310.0(1)	Maximum threshold value
$\Gamma_{\gamma 21}$	K			0.9	Minimum difference threshold value
$\Gamma_{\gamma 22}$	K			6.0	Maximum difference threshold value
$\Gamma_{\gamma 31}$	K			2.0 / 1.5(1)	Minimum difference threshold value
$\Gamma_{\gamma 32}$	K			6.0 / 5.0(1)	Maximum difference threshold value

(1) Night/twilight time value, *i.e.*, when $\theta_s > 60$

FRP Gridded assessment					
Γ_s				0.25	Minimum fraction of cloud free pixels in a grid box
C_t	hour			1.0	Duration of the FRP Gridded temporal integral
G°	degree	1.0	5.0	5.0	Resolution of the regular grid
G°_x	degree			0.0	Offset of the regular grid along the longitude
G°_y	degree			0.0	Offset of the regular grid along the latitude